Optimal-Order Switching-Aware Time Integration for Switched Process Models Governed by Semilinear Parabolic Equations

Mouloud Aoudia[a,*]

[a] *Department of Industrial Engineering, College of Engineering, Northern Border University, P.O. Box 1321, Arar 91431, Saudi Arabia.*

[*] *Corresponding author; mouloud.aoudia@nbu.edu.sa*

Submitted 01/02/2026
Accepted 26/03/2026
Published 19/07/2026
DOI: 10.64518/uohjs.2026.01

Abstract:
Semilinear parabolic equations with piecewise-in-time operators, discontinuous temporal coefficients, and switching nonlinearities are frequently used to model multiphase phenomena and regime-dependent distributed dynamics. Despite the general efficiency of standard implicit-explicit (IMEX) frameworks, applying multistep time integrators across temporal interfaces can mix values generated under different operators, potentially producing artificial transients, numerical instabilities, and a loss of asymptotic accuracy. To bridge the gap between piecewise-in-time weak formulations and practical numerical implementation, this paper formulates a switching-aware time integration framework. First, the global existence and uniqueness of an interval-wise weak solution are established by applying a Faedo-Galerkin argument on each temporal slab, transmitting the state continuously across interfaces. Second, a switching-aware baseline Crank-Nicolson method is formulated and analyzed for conditional stability. To mitigate interface artifacts and preserve the expected convergence rate, a restarted IMEX-BDF2 variant is introduced. Local truncation error analysis and the Method of Manufactured Solutions indicate that enforcing an algorithmic restart at phase boundaries prevents multistep information from crossing interfaces and maintains second-order accuracy in the reported tests. Finally, a comparative work-precision evaluation demonstrates that the proposed switching-aware scheme can provide improved computational efficiency relative to the classical methods considered here when navigating abrupt operator transitions.

Keywords*: Semilinear parabolic equations; Piecewise-in-time operators; Algorithmic restart strategy; Temporal interfaces; IMEX-BDF2; Computational efficiency.*

1. INTRODUCTION

Semilinear parabolic partial differential equations provide a standard mathematical framework for modeling diffusion-reaction phenomena, threshold dynamics, and other time-dependent distributed processes. Their analysis becomes more delicate when the governing operators lack global temporal smoothness, when material coefficients undergo abrupt changes, or when the nonlinear response is piecewise defined or subject to discrete switching laws.

Non-smooth features arise naturally in regime-dependent distributed models and in parabolic problems involving coefficient jumps, transmission interfaces, or discontinuous forcing (Dong & Xu, 2021; Feng & Shen, 1999; Vynnycky & Mitchell, 2013; Gal & Warma, 2016, 2017; Creo et al., 2022). These temporal and structural discontinuities can invalidate the smoothness assumptions implicitly used by standard multistep time-integration procedures. When numerical schemes reuse values computed at earlier time levels under fundamentally different governing operators, they may generate non-physical boundary layers in time, which can in turn affect stability and accuracy.

Over the past decade, the mathematical literature has made steady progress in extending analytical tools for low-regularity parabolic problems. In the deterministic setting, time-weighted and maximal-regularity frameworks provide well-posedness results for broad semilinear and quasilinear classes (Matioc & Walker, 2024; Schmitz & Walker, 2025; Wilke, 2023). In parallel, interface and heterogeneous-media theories have clarified transmission effects and regularity limitations induced by coefficient jumps, particularly for divergence-form operators associated with composite materials (Dong & Xu, 2021) and for nonlocal transmission across rough interfaces (Gal & Warma, 2016, 2017; Creo et al., 2022). On the numerical-analysis side, discontinuities in coefficients, data, or boundary conditions are known to trigger local consistency defects when a scheme mixes information across a discontinuity, as illustrated by finite-element results for semilinear parabolic equations with discontinuous coefficients (Feng & Shen, 1999) and by accuracy degradation under discontinuous boundary forcing (Vynnycky & Mitchell, 2013). Related analytical studies of stiff exponential and Lawson-type integrators further show that observed order degradation can be traced to stiff order conditions, local error structure, defect-based estimators, and regularity or annihilation constraints (Auzinger & Herfort, 2014; Auzinger et al., 2014, 2015; Hansen & Ostermann, 2016; Alonso-Mallo et al., 2017a, 2017b; Hochbruck et al., 2020; Cano & Reguera, 2022).

When parabolic PDEs are discretized in space, the resulting system of ordinary differential equations is often stiff. The development of stable numerical methods for such systems remains an active area of research in computational mathematics. In particular, there is continuing interest in constructing robust implicit schemes for complex diffusion-dominated and convection-diffusion-type models, including recent advances in time-space fractional equations (Edwan, 2022).

Despite the practical efficiency of standard implicit-explicit (IMEX) frameworks for stiff systems, these multistep schemes encounter mathematical and computational limitations when applied to parabolic equations with abrupt temporal discontinuities. A primary difficulty is the time-step restriction, often dictated by CFL-type conditions for the explicit components, which may become more restrictive near sudden temporal transitions (Ascher et al., 1997; Wang et al., 2023). In addition, standard multistep IMEX methods may suffer from order reduction and nonlinear decoupling at temporal interfaces. Because the implicit and explicit blocks are typically evaluated separately, abrupt switching can disturb the balance required for an accurate treatment of the nonlinear terms, leading to local truncation errors and reduced global accuracy (Kadioglu, 2017; Alonso-Mallo et al., 2017a; Hochbruck et al., 2020; Cano & Reguera, 2022). Although the stiff time-integration literature contains various IMEX and multistep strategies, including variable step-size IMEX linear multistep methods for time-dependent PDEs (Wang & Ruuth, 2008), unconditional-stability analyses for multistep ImEx constructions (Seibold et al., 2019), and variable two-step IMEX-BDF methodology for nonsmooth-in-time problems (Wang et al., 2019), these works do not explicitly target prescribed operator switching together with an interface-safe mechanism for managing carried-over multistep information.

Comparative evaluations of second-order stiff solvers further illustrate related difficulties. Although the Crank-Nicolson method is A-stable, it may exhibit weakly damped high-frequency oscillations in response to sharp initial transients and jump discontinuities, and these non-physical oscillations may persist over long integration times (Østerby, 2003). By contrast, standard BDF2 offers stronger numerical damping but may be sensitive to start-up errors and numerical instabilities when discontinuous interfaces are crossed without appropriate step-ratio control (Nishikawa, 2019; Liao & Zhang, 2021). More broadly, analyses of stiff exponential and Lawson-type integrators show that low regularity, incompatibility conditions, and local defect accumulation can alter the observed convergence order and practical damping behavior (Auzinger & Herfort, 2014; Auzinger et al., 2014, 2015; Hansen & Ostermann, 2016; Alonso-Mallo et al., 2017a, 2017b; Hochbruck et al., 2020; Cano & Reguera, 2022).

To bridge the gap between piecewise-in-time weak formulations and the practical implementation of interface-safe numerical methods, several studies have employed energy-based operator splitting and partitioned algorithms. Frameworks such as Heterogeneous Asynchronous Time Integrators (HATI) use dual Schur decompositions and Lagrange multipliers to enforce state continuity and reduce spurious pseudo-energy at discontinuous interfaces (Brun et al., 2015; Peterson et al., 2019). However, while these approaches are designed to promote energy stability, their implementation may require the solution of saddle-point systems or the evaluation of continuous penalty parameters, which can become costly for highly nonlinear parabolic systems. At the same time, studies of order reduction and order-preserving modifications in stiff integrators indicate that accuracy loss is often tied to the way stage data, quadrature structure, or stored multistep information are reused across low-regularity regimes (Alonso-Mallo et al., 2017a, 2017b; Hochbruck et al., 2020; Cano & Reguera, 2022). Recent algorithmic developments have also introduced restart ideas in multirate IMEX settings (Fish et al., 2024), suggesting that restarting may be structurally beneficial in problems with changing dynamics.

Against this background, a specific gap remains in the current literature. Existing weak theories typically address spatial heterogeneity and transmission, or globally formulated evolution with time-dependent operators under regularity assumptions that do not reflect abrupt switching. At the same time, the numerical-analysis literature has developed analytical frameworks for stiff order conditions, local error structure, defect-based estimators, and order-reduction avoidance in smooth-regime stiff integrators (Auzinger & Herfort, 2014; Auzinger et al., 2014, 2015; Hansen & Ostermann, 2016; Alonso-Mallo et al., 2017a, 2017b; Hochbruck et al., 2020; Cano & Reguera, 2022), but these analyses are not formulated around prescribed temporal operator switching and the cross-interface reuse of past multistep values. Standard stiff integrators and IMEX multistep schemes generally assume a single regime, or at least smooth time dependence, so that the multistep stencil may safely reuse past values. In a switching model, however, the stencil may cross a genuine temporal interface, creating a local modeling mismatch in which values generated under different operators are algebraically mixed.

The present paper addresses this gap by aligning the continuous notion of solution transmission at switching times with an algorithmic restart rule that prevents multistep or multistage information from being carried across interfaces. To do so, we formulate a piecewise-in-time variational model with prescribed switching times and define an interval-wise weak solution transmitted continuously in the pivot space H at every switching instant t_m. Under uniform ellipticity together with global Lipschitz and energy-control hypotheses, we prove existence on each slab by the Faedo-Galerkin method and obtain global existence and uniqueness by concatenation with H-continuity at switching times. We then introduce a switching-aware time-integration principle that enforces each switching time as an exact time node and restarts the time integrator at t_m, thereby reducing cross-interface reuse of past-step information. To implement this principle, we develop an interval-wise Crank-Nicolson discretization and establish discrete solvability, conditional stability, and convergence on a switching-aware grid. Finally, we present a restarted IMEX-BDF2 variant, bootstrapped by one Crank-Nicolson step on each interval, as a computational alternative designed for switching contexts; its role in the present paper is primarily algorithmic and validation-based rather than that of a complete standalone convergence theory.

The remainder of the paper is organized as follows. Section 2 introduces the model class, the variational setting, and the piecewise weak formulation. Section 3 establishes interval-wise well-posedness and global continuation. Section 4 derives switching-aware discretizations. Section 5 analyzes the baseline Crank-Nicolson method. Section 6 reports verification and validation experiments illustrating the interface-safe behavior of the restarted strategy. Section 7 discusses the findings in relation to the literature. Section 8 presents the limitations of the present study together with directions for future research. Section 9 concludes the paper.

2. MODEL CLASS, FUNCTIONAL SETTING, AND WEAK FORMULATION

This section formulates the analytical class of problems addressed in this paper. The governing equations considered here accommodate temporal irregularities and spatial transmission constraints within a standard variational setting.

2.1. Geometric and Temporal Decomposition

Let the spatial domain $\Omega \subset \mathbb{R}^d$, with spatial dimension $d \geq 1$, be a bounded, open, and connected set equipped with a sufficiently regular boundary $\partial\Omega$. To account for heterogeneous material properties, we assume that the global domain Ω is decomposed into a finite, disjoint family of non-overlapping open subdomains Ω_r. To correctly account for internal interfaces covering the full domain, we express this decomposition formally using closures:

$$\overline{\Omega} = \bigcup_{r=1}^{R} \overline{\Omega}_r, \qquad \Omega_r \cap \Omega_s = \emptyset \quad \text{for } r \neq s \tag{1}$$

The internal boundaries of these interacting subdomains generate a static spatial interface set, denoted by Γ, which is defined as the union of all shared subdomain boundaries:

$$\Gamma := \bigcup_{r \neq s} (\partial\Omega_r \cap \partial\Omega_s) \tag{2}$$

Let the global temporal domain $[0, T]$ be partitioned by a set of prescribed, discrete switching times representing the moments of operational regime change:

$$0 = t_0 < t_1 < \cdots < t_M = T \tag{3}$$

This partition generates M distinct, open temporal subintervals, defined mathematically as half-open sets to ensure strict non-overlap of the operative regimes:

$$I_m \coloneqq (t_{m-1}, t_m], \qquad m = 1, \dots, M \tag{4}$$

2.2. Piecewise-in-Time Semilinear Transmission Model

We consider an unknown scalar state field $u: \Omega \times [0, T] \to \mathbb{R}$ that satisfies, on each isolated temporal subinterval I_m and within each specific spatial subdomain Ω_r, a semilinear parabolic partial differential equation of the general form:

$$\partial_t u + \mathcal{A}_{m,r} u + \mathcal{N}_{m,r}(u) = f_{m,r} \quad \text{in } \Omega_r \times I_m \tag{5}$$

It is worth mentioning how global forcing is assembled from these subdomain sources. If the model is given by subdomain sources $f_{m,r}$ on Ω_r, we define the globally assembled forcing $f_m \in L^2(I_m; V')$ by:

$$\langle f_m(t), \phi \rangle_{V',V} := \sum_{r=1}^{R} \int_{\Omega_r} f_{m,r}(x, t)\, \phi(x)\, dx, \qquad \forall \phi \in V, \text{ a.e. } t \in I_m \tag{6}$$

The active linear elliptic operator is written in divergence form:

$$\mathcal{A}_{m,r} u = -\nabla \cdot \big(K_{m,r}(x) \nabla u\big) + c_{m,r}(x) u \tag{7}$$

Here, $K_{m,r}(x)$ represents a spatially dependent symmetric diffusion tensor that is defined consistently on each interval I_m but may undergo instantaneous jumps at the explicit switching times t_m. The term $c_{m,r}(x)$ operates as a lower-order reaction or dissipation coefficient.

To mathematically encode switching nonlinearities, we introduce a discrete switching map σ:

$$\sigma: \{1, \dots, M\} \to \{1, \dots, S\}, \tag{8}$$

which selects, for each interval I_m, one specific nonlinear law from a predefined finite analytical library $\{\mathcal{G}_1, \dots, \mathcal{G}_S\}$. The active nonlinear response enforced on the specific interval is evaluated locally as $\mathcal{N}_{m,r}(u) = \mathcal{G}_{\sigma(m),r}(u)$.

For the global weak formulation, we define the assembled nonlinear operator $\mathcal{G}_{\sigma(m)}: V \to V'$ by gathering the subdomain-wise contributions:

$$\langle \mathcal{G}_{\sigma(m)}(u), \phi \rangle_{V',V} := \sum_{r=1}^{R} \int_{\Omega_r} \mathcal{G}_{\sigma(m),r}\,(u|_{\Omega_r})\, \phi|_{\Omega_r}\, dx, \qquad \forall \phi \in V. \tag{9}$$

2.3. External Boundary and Transmission Conditions

To ensure that the theoretical analysis and the subsequent numerical verification remain mathematically coherent, we impose homogeneous Dirichlet boundary conditions across the entirety of the external boundary:

$$u(x,t) = 0 \quad \text{on } \partial\Omega \times (0,T]. \tag{10}$$

Across each internal interface segment $\partial\Omega_r \cap \partial\Omega_s \subset \Gamma$, we enforce standard physical transmission requirements consisting of continuity of the state variable and the balance of the normal diffusive flux:

$$u_r \quad = u_s \quad \text{on } \Gamma \times I_m, \tag{11}$$

$$\left(K_{m,r}\nabla u_r\right) \cdot \mathrm{n}_r + \left(K_{m,s}\nabla u_s\right) \cdot \mathrm{n}_s \quad = 0 \quad \text{on } \Gamma \times I_m, \tag{12}$$

where n_r and n_s represent the outward-pointing unit normal vectors relative to the subdomains Ω_r and Ω_s.

Regarding the transmission conditions in the variational setting, it is important to note that since $u \in H_0^1(\Omega)$ has a single trace on any sufficiently regular internal interface, the continuity condition (11) on Γ is automatically encoded by the choice $V = H_0^1(\Omega)$. The flux balance condition (12) on $\Gamma \times I_m$ is interpreted in a weak (distributional) sense through integration by parts in the bilinear form $a_m(\cdot,\cdot)$. A classical pointwise flux balance is recovered only under additional piecewise regularity, e.g., $u|_{\Omega_r} \in H^2(\Omega_r)$.

2.4. Functional Setting

We designate the standard Gelfand triple by defining the functional spaces and their dense and continuous embeddings in a single unified structure:

$$V := H_0^1(\Omega), \quad H := L^2(\Omega), \quad V' := \left(H_0^1(\Omega)\right)', \qquad V \hookrightarrow H \hookrightarrow V'. \tag{13}$$

The duality pairing acting between V' and V is denoted by $\langle \cdot,\cdot \rangle_{V',V}$, and the standard L^2 inner product on the pivot space H is denoted by $(\cdot,\cdot)_H$.
For each temporal subinterval I_m, the bilinear form $a_m: V \times V \to \mathbb{R}$ corresponding to the globally assembled linear elliptic operator $\mathcal{A}_{m,r}$ is defined via standard integration by parts over the disjoint subdomains:

$$a_m(u,\phi) := \sum_{r=1}^{R} \int_{\Omega_r} \left(\nabla\phi^\top K_{m,r}(x)\nabla u + c_{m,r}(x) u\phi\right) dx, \qquad \forall u, \phi \in V. \tag{14}$$

2.5. Structural Assumptions

We introduce the following structural assumptions to ensure that the piecewise-in-time weak formulation admits the required passage to the limit.

- ***Assumption A 2.1 (Uniform Ellipticity):*** For each interval m and subdomain r, $K_{m,r}(x)$ is Lebesgue measurable. There exist global bounding constants $\lambda, \Lambda > 0$, independent of m and r, such that:

$$\lambda|\xi|^2 \leq \xi^\top K_{m,r}(x)\xi \leq \Lambda|\xi|^2 \quad \text{for a.e. } x \in \Omega_r,\ \forall \xi \in \mathbb{R}^d. \tag{15}$$

- ***Assumption A 2.2 (Lower-Order Control):*** The lower-order reaction coefficients $c_{m,r}$ belong to $L^\infty(\Omega_r)$, and there exists a uniform scalar constant $c^* \in \mathbb{R}$ such that $c_{m,r}(x) \geq c^*$ almost everywhere in Ω_r.
- ***Assumption A 2.3 (Admissible Forcing):*** For each discrete interval m, the globally assembled external source term f_m satisfies $f_m \in L^2(I_m; V')$.
- ***Assumption A 2.4 (Nonlinearity - Lipschitz & Energy Control):*** For each active operational phase m, the globally assembled nonlinear operator $\mathcal{G}_{\sigma(m)}: H \to V'$ satisfies:
  - *Global Lipschitz:*

$$\| \mathcal{G}_{\sigma(m)}(v) - \mathcal{G}_{\sigma(m)}(w) \|_{V'} \leq L_G \| v - w \|_H \quad \forall v, w \in H. \tag{16}$$

  - *Linear growth:*

$$\| \mathcal{G}_{\sigma(m)}(v) \|_{V'} \leq C_G(1 + \| v \|_H) \quad \forall v \in H. \tag{17}$$

  - *One-sided energy control:*

$$\langle \mathcal{G}_{\sigma(m)}(v), v \rangle_{V',V} \geq -\gamma_0 - \gamma_1 \| v \|_H^2 \quad \forall v \in V. \tag{18}$$

- ***Assumption A 2.5 (Temporal Switching Compatibility):*** At each explicitly defined switching time t_m, the state variable is strictly required to be continuous relative to the pivot space H:

$$u(t_m^-) = u(t_m^+) \quad \text{in } H, \qquad \forall m = 1, \dots, M-1. \tag{19}$$

At this point, it is necessary to address the distinction between local Lipschitz properties and practical truncation. Although Assumption A 2.4 postulates a global Lipschitz mapping $H \to V'$, many physical nonlinearities (e.g., quadratic reaction terms such as Lotka-Volterra) are only locally Lipschitz. A standard rigorous device is to introduce a truncated nonlinearity $G_{\sigma_m,R}$ such that $G_{\sigma_m,R}(v) = G_{\sigma_m}(v)$ whenever $\| v \|_{L^\infty(\Omega)} \leq R$, and $G_{\sigma_m,R}$ is globally Lipschitz from H into V'. If an a priori bound guarantees $\| u(t) \|_{L^\infty(\Omega)} \leq R$ for all $t \in (0, T]$, then $G_{\sigma_m,R}\big(u(t)\big) = G_{\sigma_m}\big(u(t)\big)$ for all $t \in (0, T]$, so the truncated and original problems coincide on the true solution trajectory. Consequently, one may conduct the weak existence/uniqueness analysis using $G_{\sigma_m,R}$ without altering the physical solution.

2.6. Weak Formulation

Definition 2.1 (Piecewise Weak Solution). A function $u \in L^2(0, T; V)$ is called a piecewise weak solution if it satisfies the following criteria: For each temporal subinterval I_m, the solution restricts to the local regularity class:

$$u|_{I_m} \in L^2(I_m; V) \cap C\big(\bar{I}_m; H\big). \tag{20}$$

For all admissible test functions $\phi \in V$, and for almost every $t \in I_m$, the weak integral equation holds:

$$\langle \partial_t u(t), \phi \rangle_{V',V} + a_m(u(t), \phi) + \langle \mathcal{G}_{\sigma(m)}(u(t)), \phi \rangle_{V',V} = \langle f_m(t), \phi \rangle_{V',V}. \quad (21)$$

The global initial condition is satisfied, $u(0) = u_0$ in H, and the temporal matching condition (19) holds at all interior interfaces t_m.

Having specified the mathematical model, the domains, and the structural assumptions, we now have the variational framework needed for the existence analysis. In particular, the uniform ellipticity (A 2.1) and one-sided energy control (A 2.4) yield the coercivity bounds required for the a priori estimates. In the following section, these properties are used within a Faedo-Galerkin framework to prove the existence of a local weak solution on each time slab, which is then concatenated to obtain the global piecewise solution.

3. WEAK WELL-POSEDNESS, INTERVAL-WISE CONTINUATION, AND UNIQUENESS

Having established the structural assumptions, we now detail the analytical proofs demonstrating that the piecewise-in-time weak problem is globally well-posed through interval-wise estimates and continuation.

3.1. Preliminary Estimates and Local Existence

Lemma 3.1 (Boundedness and Gårding Inequality). *Under Assumptions A 2.1 - A 2.2, for each interval index m, there exist structural constants $C_a > 0$, $\alpha > 0$, and $\beta \geq 0$, independent of m, such that the spatial bilinear form a_m satisfies:*

$$|a_m(v, \phi)| \leq C_a \| v \|_V \| \phi \|_V \quad \forall v, \phi \in V,$$
$$a_m(v, v) \geq \alpha \| v \|_V^2 - \beta \| v \|_H^2 \quad \forall v \in V.$$

Proof.

The continuity part of the lemma follows directly from applying the standard Cauchy-Schwarz inequality over each subdomain Ω_r bounded by the essential supremums of $K_{m,r}$ and $c_{m,r}$. For the coercivity bound (22), the uniform ellipticity condition guarantees:

$$\sum_{r=1}^{R} \int_{\Omega_r} \nabla v^\top K_{m,r} \nabla v \, dx \geq \lambda \| \nabla v \|_{L^2(\Omega)}^2. \quad (22)$$

By Poincaré's inequality on $V = H_0^1(\Omega)$, this yields control of the V-norm. Utilizing $c_{m,r}(x) \geq c^*$, we observe:

$$\sum_{r=1}^{R} \int_{\Omega_r} c_{m,r}(x) v^2 \, dx \geq c^* \| v \|_H^2. \quad (23)$$

If $c^* < 0$, one obtains the stated Gårding inequality by choosing suitable constants $\alpha > 0$ and $\beta = -c^* > 0$. □

Theorem 3.1 (Interval-Wise Existence on a Single Time Slab). *Fix $m \in \{1, \dots, M\}$ and let a valid incoming initial state $u_{m-1} \in H$ be given. Under Assumptions A 2.1–A 2.4, there exists a function $u_m \in L^2(I_m; V) \cap C(\overline{I}_m; H)$,* with $\partial_t u_m \in L^2(I_m; V')$, *that satisfies the weak formulation (21) for all allowable test functions $\phi \in V$ almost everywhere in I_m, subject to $u_m(t_{m-1}) = u_{m-1}$ in H.*

Proof.

We utilize the Faedo-Galerkin approximation method. Let $\{w_k\}_{k \geq 1}$ be a countable basis of V orthonormal in H. For any fixed integer $N \geq 1$, define the subspace $V_N := \text{span}\{w_1, \dots, w_N\}$. We seek an approximate solution of the form:

$$u_N(t)=\sum_{k=1}^{N} d_k^N\,(t)w_k, \tag{24}$$

by projecting the governing PDE onto V_N using the defined duality pairings:

$$\left(\partial_t u_N(t),w_j\right)_H+a_m\left(u_N(t),w_j\right)+\langle\mathcal{G}_{\sigma(m)}\left(u_N(t)\right),w_j\rangle_{V',V}=\langle f_m(t),w_j\rangle_{V',V}, \tag{25}$$

for all $j=1,\dots,N$. The initial condition is the H-orthogonal projection of u_{m-1} onto V_N. Because $\mathcal{G}_{\sigma(m)}$ satisfies the Lipschitz condition mapping into V' (16), the resulting ODE system is continuous and locally Lipschitz, possessing a unique local solution by the standard Picard-Lindelöf theorem.
To extend this solution globally over I_m, we derive *a priori* estimates. Multiplying the j-th equation by $d_j^N(t)$ and summing from $j=1$ to N yields:

$$(\partial_t u_N,u_N)_H+a_m(u_N,u_N)+\langle\mathcal{G}_{\sigma(m)}(u_N),u_N\rangle_{V',V}=\langle f_m,u_N\rangle_{V',V}. \tag{26}$$

Applying $\langle\partial_t u_N,u_N\rangle_H=\frac{1}{2}\frac{d}{dt}\parallel u_N\parallel_H^2$, the Gårding inequality (22), and the one-sided energy control (18), we establish the lower bounds:

$$\frac{1}{2}\frac{d}{dt}\parallel u_N\parallel_H^2+\alpha\parallel u_N\parallel_V^2-\beta\parallel u_N\parallel_H^2-\gamma_0-\gamma_1\parallel u_N\parallel_H^2\leq\langle f_m,u_N\rangle_{V',V}. \tag{27}$$

By explicitly applying Young's inequality, the right-hand side satisfies $\langle f_m,u_N\rangle_{V',V}\leq\frac{1}{2\alpha}\parallel f_m\parallel_{V'}^2+\frac{\alpha}{2}\parallel u_N\parallel_V^2$. Absorbing the resulting $\frac{\alpha}{2}\parallel u_N\parallel_V^2$ into the left-hand side yields the fundamental inequality:

$$\frac{d}{dt}\parallel u_N\parallel_H^2+\alpha\parallel u_N\parallel_V^2\leq 2(\beta+\gamma_1)\parallel u_N\parallel_H^2+2\gamma_0+\frac{1}{\alpha}\parallel f_m\parallel_{V'}^2. \tag{28}$$

Applying Gronwall's lemma over (t_{m-1},t), we obtain that $\parallel u_N(t)\parallel_H^2$ is bounded independently of the dimension N for all $t\in I_m$. Integrating (28) over I_m provides the first required uniform stability bound in the relevant spaces:

$$\sup_{t\in I_m}\parallel u_N(t)\parallel_H^2+\int_{I_m}\parallel u_N(t)\parallel_V^2\;dt\leq C. \tag{29}$$

To bound the time derivative, we project (27) onto an arbitrary vector $v\in V$ with $\parallel v\parallel_V\leq 1$. Utilizing bounds (21) and (16), we obtain the second mandatory bound defining the time derivative:

$$\int_{I_m}\parallel\partial_t u_N(t)\parallel_{V'}^2\;dt\leq C'. \tag{30}$$

Estimates (29) and (30) show that the Galerkin sequence $\{u_N\}$is bounded in the space $W(I_m):=\{u\in L^2(I_m;V):\partial_t u\in L^2(I_m;V')\}$. By deploying the Aubin-Lions compactness lemma and standard Banach-Alaoglu principles, we extract a convergent subsequence (not relabeled) and a limit function u_m satisfying the following convergences:

$$u_N\ \overset{*}{\rightharpoonup}\ u_m\quad\text{weakly-* in } L^\infty(I_m;H), \tag{31}$$

$$u_N\ \rightharpoonup\ u_m\quad\text{weakly in } L^2(I_m;V), \tag{32}$$

$$\partial_t u_N \rightharpoonup \partial_t u_m \quad \text{weakly in } L^2(I_m; V'), \tag{33}$$

$$u_N \to u_m \quad \text{strongly in } L^2(I_m; H). \tag{34}$$

Using the strong convergence established in (34) together with the global Lipschitz assumption (16), we now pass to the limit in the nonlinear term:

$$\int_{I_m} \| \mathcal{G}_{\sigma(m)}(u_N) - \mathcal{G}_{\sigma(m)}(u_m) \|_{V'}^2 \, dt \le L_G^2 \int_{I_m} \| u_N(t) - u_m(t) \|_H^2 \, dt. \tag{35}$$

Since the right-hand integral converges to 0 as $N \to \infty$, it follows that $\mathcal{G}_{\sigma(m)}(u_N) \to \mathcal{G}_{\sigma(m)}(u_m)$ strongly in $L^2(I_m; V')$. This rigorous limit allows us to safely pass to the limit within all combined terms of (27), confirming that $u_m$satisfies the weak formulation (21) on I_m. □

3.2. Global Continuation and Uniqueness

Theorem 3.2 (Global Piecewise-in-Time Existence). *Under the assumptions of Theorem 3.1 and Assumption A 2.5, there exists a global piecewise weak solution* $u \in L^2(0,T;V) \cap C([0,T];H)$ *obtained by concatenating the interval solutions* u_m.

Proof.

Applying Theorem 3.1 on I_1 with $u(0) = u_0$ yields a well-defined terminal state $u_1(t_1)$. By Assumption A 2.5, we define this exact state as the initial condition for I_2. Iterating this procedure over all M intervals naturally produces a continuous, piecewise solution on $[0,T]$. □

Theorem 3.3 (Uniqueness and Continuous Dependence). *If* u *and* v *are solutions corresponding to initial data* u_0, v_0 *and source terms* f, g*, then for all* $t \in [0,T]$*:* $\| u(t) - v(t) \|_H^2 \le C_T \left(\| u_0 - v_0 \|_H^2 + \| f - g \|_{L^2(0,T;V')}^2 \right)$. *Consequently, the piecewise weak solution is uniquely determined.*

Proof.

Define the variable $z(t) := u(t) - v(t)$. Subtracting the weak formulations on I_m and testing directly with the algebraic definition $\phi = z(t)$ yields:

$$\frac{1}{2}\frac{d}{dt} \| z \|_H^2 + a_m(z,z) + \langle \mathcal{G}_{\sigma(m)}(u) - \mathcal{G}_{\sigma(m)}(v), z \rangle_{V',V} = \langle f - g, z \rangle_{V',V}. \tag{36}$$

Using the stated Gårding inequality (22) and formally bounding the nonlinear difference via Assumption A 2.4 as $\langle G_{\sigma_m}(u) - G_{\sigma_m}(v), z \rangle_{V',V} \le L_G \| z \|_H \| z \|_V$, we explicitly apply Young's inequality on the components:

$$\begin{aligned} \frac{1}{2}\frac{d}{dt} \| z \|_H^2 + \alpha \| z \|_V^2 \le \beta \| z \|_H^2 + \frac{L_G^2}{2\alpha} \| z \|_H^2 \\ + \frac{\alpha}{4} \| z \|_V^2 + \frac{1}{\alpha} \| f - g \|_{V'}^2 + \frac{\alpha}{4} \| z \|_V^2. \end{aligned} \tag{37}$$

Subtracting precisely $\frac{\alpha}{2} \| z \|_V^2$ from both sides, the remaining formal V-norm remains universally positive and can therefore be rigorously discarded:

$$\frac{d}{dt} \| z \|_H^2 \le \left(2\beta + \frac{L_G^2}{\alpha} \right) \| z \|_H^2 + \frac{2}{\alpha} \| f - g \|_{V'}^2. \tag{38}$$

Applying Gronwall's lemma on I_1yields a bound up to t_1. Since the state is transmitted continuously in H at each switching time (Assumption A 2.5, $z(t_m^-) = z(t_m^+)$), the estimate extends interval by interval over $[0, T]$. □

The establishment of global existence and uniqueness relies on the H-continuity condition at the interfaces, which specifies how the state is transmitted between consecutive operators. This transmission principle motivates the numerical strategy developed in the next section. To avoid blending values generated under different regimes, the discretization enforces switching times as exact grid nodes and restarts the time integrator at those points, thereby reducing cross-interface contamination.

4. NUMERICAL DISCRETIZATION AND SWITCHING-AWARE TIME INTEGRATION

To prevent multistep or multistage solvers from bridging switching interfaces and mixing values generated under different operators, we formulate a discretization strategy in which all prescribed switching times are treated as exact grid nodes and the time integrator is restarted at these points. We first analyze a switching-aware Crank-Nicolson method and then present a restarted IMEX-BDF2 variant.

4.1. Spatial Semidiscretization (Conforming FE)

Let $\mathcal{T}_h$ denote a shape-regular mesh resolving the domain Ω. and the internal boundaries separating $\{\Omega_r\}_{r=1}^{R}$. Let $V_h \subset V$ represent a conforming finite-element space of continuous piecewise polynomials scaled to degree $p \geq 1$.

We denote by $V_h{}'$ the algebraic dual of V_h and explicitly utilize the induced duality pairing $\langle\cdot,\cdot\rangle_{V_h{}',V_h}$. Within computational implementations, $V_h{}'$ is represented via the mass matrix. To ensure stability constants remain independent of the mesh scale h, we explicitly equip the algebraic dual $V_h{}'$ with the discrete dual norm:

$$\| l \|_{V_h{}'} := \sup_{\phi_h \in V_h, \phi_h \neq 0} \frac{\langle l, \phi_h \rangle_{V_h{}',V_h}}{\| \phi_h \|_V}. \tag{39}$$

For each temporal slab $I_m = (t_{m-1}, t_m]$, we introduce the semidiscrete linear operator mapping explicitly $\mathcal{A}_{m,h}: V_h \to V_h{}'$ defined strictly via the associated spatial bilinear form:

$$\langle \mathcal{A}_{m,h} w_h, \phi_h \rangle_{V_h{}',V_h} = a_m(w_h, \phi_h) \quad \forall w_h, \phi_h \in V_h. \tag{40}$$

The corresponding semidiscrete nonlinear operator $G_{m,h}: V_h \to V_h'$ is defined by:

$$\langle \mathcal{G}_{m,h} w_h, \phi_h \rangle_{V_h{}',V_h} = \langle \mathcal{G}_{\sigma(m)}(w_h), \phi_h \rangle_{V',V} \quad \forall w_h, \phi_h \in V_h. \tag{41}$$

Finally, the discrete forcing term $f_{m,h}(t) \in V_h'$is defined by restriction to V_h:

$$\langle f_{m,h}(t), \phi_h \rangle_{V_h{}',V_h} := \langle f_m(t), \phi_h \rangle_{V',V} \quad \forall \phi_h \in V_h. \tag{42}$$

4.2. Discrete Hypotheses on V_h

We assume that, on each interval, the discrete operators satisfy discrete counterparts of the continuous structural bounds:

- ***D 4.1 (Continuity):*** $|a_m(v_h, w_h)| \leq C_a \| v_h \|_V \| w_h \|_V \quad \forall v_h, w_h \in V_h$.
- ***D 4.2 (Gårding/Coercivity):*** $a_m(v_h, v_h) \geq \alpha \| v_h \|_V^2 - \beta \| v_h \|_H^2 \quad \forall v_h \in V_h$.
- ***D 4.3 (Lipschitz nonlinearity)*:** $\| \mathcal{G}_{m,h}(v_h) - \mathcal{G}_{m,h}(w_h) \|_{V_h{}'} \leq L_G \| v_h - w_h \|_H \;\; \forall v_h, w_h \in V_h$.
- ***D 4.4 (Growth)*:** $\| \mathcal{G}_{m,h}(v_h) \|_{V_h{}'} \leq C_G(1 + \| v_h \|_H) \quad \forall v_h \in V_h$.

Here, $\langle\cdot,\cdot\rangle_{V_h{}',V_h}$ denotes the duality pairing induced by the mass matrix (or any equivalent norm on the finite-dimensional space), and $(\cdot,\cdot)_H$ is the standard L^2 inner product.

4.3. Switching-Aware Temporal Grid

Given the switching partition $0 = t_0 < t_1 < \cdots < t_M = T$, we introduce a local temporal mesh on each interval I_m:

$$t_{m,0} = t_{m-1} < t_{m,1} < \cdots < t_{m,N_m} = t_m, \qquad \tau_{m,n} = t_{m,n+1} - t_{m,n}. \tag{43}$$

The partition points $\{t_m\}_{m=0}^{M}$represent genuine discontinuities in the active operators. Accordingly, each switching time is treated as an exact grid node. If a multistep stencil crosses t_m, then values generated under different regimes are mixed, which can introduce a local consistency defect and artificial temporal transients. We therefore construct the grid so that every t_m is a time node and restart the time integrator at t_m: $U_{m+1}^0 = U_m^{N_m}$, thereby preventing cross-interface reuse of the discrete history.

The Crank-Nicolson scheme is analyzed first because, as a one-step method, it requires only the previous state value and is therefore naturally compatible with switching interfaces and the transmission condition. Its conditional stability and convergence analysis provide the baseline theoretical foundation before the multistep variant is introduced.

4.4. Baseline Analyzed Scheme: Interval-Wise Crank-Nicolson

For the baseline fully discrete model, we deploy a one-step, second-order Crank-Nicolson discretization. Denoting the numerical approximation at $t_{m,n}$ by $U_m^n \in V_h$, the scheme is defined as follows: find $U_m^{n+1} \in V_h$ such that for all test vectors $\phi_h \in V_h$:

$$\begin{aligned}\left(\frac{U_m^{n+1} - U_m^n}{\tau_{m,n}}, \phi_h\right)_H &+ a_m\left(\frac{U_m^{n+1} + U_m^n}{2}, \phi_h\right)\\ +\frac{1}{2}\langle \mathcal{G}_{m,h}(U_m^{n+1}) + \mathcal{G}_{m,h}(U_m^n), \phi_h\rangle_{V_h',V_h} &= \langle f_{m,h}\big(t_{m,n+1/2}\big), \phi_h\rangle_{V_h',V_h},\end{aligned} \tag{44}$$

where $t_{m,n+1/2} = t_{m,n} + \tau_{m,n}/2$. The integration sequence is cleanly restarted at explicit switching times via:

$$U_{m+1}^0 = U_m^{N_m}, \qquad \forall m = 1, \ldots, M-1. \tag{45}$$

Lemma 4.1 (Discrete solvability of one Crank-Nicolson step). *Fix an interval I_m and a time step $\tau_{m,n} >$ 0. Assume D 4.2 – D 4.3. Then there exists $\tau_{solv} > 0$ depending only on α, β, L_G (and on fixed norm-equivalence constants on V_h) such that if $0 < \tau_{m,n} \le \tau_{solv}$, the nonlinear Crank-Nicolson equation (44) admits a unique solution $U_m^{n+1} \in V_h$.*

Proof.

Write (44) at step m, n as: find $w \in V_h$ such that $\mathcal{B}(w) = 0$ in V_h', where the operator $B: V_h \to V_h'$is defined by

$$\mathcal{B}(w) := \frac{1}{\tau_{m,n}} w + \frac{1}{2}\mathcal{A}_{m,h} w + \frac{1}{2}\mathcal{G}_{m,h}(w) - F, \tag{46}$$

and $F \in V_h'$ collects the known terms involving U_m^n and $f_{m,h}$.

Let $v, w \in V_h$. Testing the difference with $v - w \in V_h$ yields

$$\begin{aligned}&\langle \mathcal{B}(v) - \mathcal{B}(w),\ v - w\rangle_{V_h',V_h}\\ &= \frac{1}{\tau_{m,n}} \| v - w \|_H^2 + \frac{1}{2} a_m(v - w, v - w) + \frac{1}{2}\langle \mathcal{G}_{m,h}(v) - \mathcal{G}_{m,h}(w),\ v - w\rangle_{V_h',V_h}.\end{aligned} \tag{47}$$

Using the required coercivity mapping (D 4.2) on a_m gives $\frac{1}{2} a_m(v - w, v - w) \ge \frac{\alpha}{2} \| v - w \|_V^2 - \frac{\beta}{2} \| v - w \|_H^2$. For the nonlinear expression, utilizing applied duality and maintaining Lipschitz limits (D3),

$$\frac{1}{2}\langle \mathcal{G}_{m,h}(v) - \mathcal{G}_{m,h}(w), v - w\rangle_{V_h{}',V_h} \\ \leq \frac{1}{2} \parallel \mathcal{G}_{m,h}(v) - \mathcal{G}_{m,h}(w) \parallel_{V_h{}'} \parallel v - w \parallel_V \leq \frac{L_G}{2} \parallel v - w \parallel_H \parallel v - w \parallel_V. \tag{48}$$

Apply Young's inequality with parameter $\varepsilon > 0$:

$$\frac{L_G}{2} \parallel v - w \parallel_H \parallel v - w \parallel_V \leq \varepsilon \parallel v - w \parallel_V^2 + \frac{L_G^2}{16\varepsilon} \parallel v - w \parallel_H^2. \tag{49}$$

Therefore, combining these terms yields:

$$\langle \mathcal{B}(v) - \mathcal{B}(w), v - w\rangle_{V_h{}',V_h} \\ \geq \left(\frac{1}{\tau_{m,n}} - \frac{\beta}{2} - \frac{L_G^2}{16\varepsilon}\right) \parallel v - w \parallel_H^2 + \left(\frac{\alpha}{2} - \varepsilon\right) \parallel v - w \parallel_V^2. \tag{50}$$

Choose $\varepsilon = \alpha/4$ so that $\frac{\alpha}{2} - \varepsilon = \alpha/4 > 0$. Then subsequently specify defining limit $\tau_{solv} > 0$ such that

$$\frac{1}{\tau_{solv}} > \frac{\beta}{2} + \frac{L_G^2}{4\alpha}. \tag{51}$$

For any $0 < \tau_{m,n} \leq \tau_{solv}$, the operator $B$is strongly monotone and continuous on the finite-dimensional space V_h. Hence it is coercive and bijective, and the existence and uniqueness of U_m^{n+1}follow from the Browder-Minty theorem. □

It is crucial to highlight the implicit nonlinearity and its corresponding discrete solvability constraint here. The Crank-Nicolson step is nonlinear because the term $\mathcal{G}_{m,h}(U_m^{n+1})$ is implicit. In practice, one computes U_m^{n+1} by a Newton method or a fixed-point iteration. Mathematically, uniqueness of the discrete solution is ensured under a (typically mild) step-size restriction that allows the coercive part of the linear operator to dominate the Lipschitz constant of $\mathcal{G}_{m,h}$; equivalently, the discrete operator defining the left-hand side becomes strongly monotone. This restriction is consistent with the conditional stability threshold derived later in the energy estimate.

4.5. Practical Variant (Numerically Assessed): Restarted IMEX-BDF2

Before detailing the multistep variant, it is important to note why one-step methods are naturally compatible with switching. Because one-step methods such as Crank-Nicolson require only the solution at the previous time node, they can smoothly transition across a switching time by enforcing the interface as a grid node and restarting with the continuity initialization. In contrast, multistep methods (e.g., BDF2) require multiple past values; therefore, at a switching time one must reset the multistep history and reinitialize the method so that the stencil does not cross the temporal interface. This distinction is consistent with the broader literature on order reduction, restart or avoidance mechanisms, and history-sensitive stiff integration (Alonso-Mallo et al., 2017a, 2017b; Hochbruck et al., 2020; Cano & Reguera, 2022). Classical BDF2 is A-stable and exhibits stronger practical damping than Crank-Nicolson, but it is not L-stable.

To obtain a favorable work-precision balance in stiff regimes, we formulate an interval-wise restarted IMEX-BDF2 scheme. On each active interval I_m, we use a uniform local time step profile:

$$\tau_{m,n} \equiv \tau_m, \qquad \text{for } n = 0, \dots, N_m - 1. \tag{52}$$

It is worth mentioning the uniform step size requirement for classical BDF2 coefficients. The standard BDF2 formula with fixed coefficients $(3U_m^{n+1} - 4U_m^n + U_m^{n-1})/(2\tau_m)$ is second-order accurate only on a uniform grid. If variable time steps are used, the BDF2 coefficients must be modified using step-ratio-dependent weights. Therefore, in the restarted IMEX-BDF2 variant we enforce a uniform step size $\tau_{m,n} \equiv \tau_m$ within each interval I_m; otherwise a variable-step BDF2 construction is required.

At the beginning of each subinterval I_m, the algorithm performs one Crank-Nicolson step to initialize U_m^1. Thereafter, for all interior indices $n \geq 1$ within I_m, the state is advanced by:

$$\left(\frac{3U_m^{n+1} - 4U_m^n + U_m^{n-1}}{2\tau_m}, \phi_h\right)_H + a_m(U_m^{n+1}, \phi_h) + \langle 2G_{m,h}(U_m^n) - G_{m,h}(U_m^{n-1}), \phi_h \rangle_{V_h{}', V_h} = \langle f_{m,h}(t_{m,n+1}), \phi_h \rangle_{V_h{}', V_h}. \quad (53)$$

Mandatory Restart Rule: Approaching an interface marker t_m, the method completes its final local run. Upon entering I_{m+1}, the stored multistep data are discarded, U_{m+1}^0 is synchronized with $U_m^{N_m}$, and the initial Crank-Nicolson bootstrap step is re-deployed to evaluate U_{m+1}^1.

With the switching-aware temporal grid in place and the discrete operator bounds specified, it remains to establish the main properties of the baseline scheme. As a one-step method, Crank-Nicolson is naturally compatible with switching times treated as grid nodes and does not require multistep information to cross interfaces. However, its implicit nonlinear term requires a conditional stability analysis. The following section establishes these bounds.

5. DISCRETE STABILITY AND CONVERGENCE ANALYSIS (BASELINE CN)

In this section we establish the main mathematical properties of the baseline Crank-Nicolson scheme, with emphasis on its conditional stability in the presence of switching nonlinearities.

5.1. Interval-Wise Conditional Stability

Theorem 5.1 (Interval-Wise Conditional Stability of CN). *Under hypotheses D 4.1 – D 4.4, define* $\tau^\star := \min\{\tau_{solv}, \tau_{stab}\}$ *where* τ_{stab} *depends uniquely on the internal constants* α, β, L_G, C_G. *If* $\tau_{m,n} \leq \tau^\star$ *everywhere on* I_m, *the formulated CN solution satisfies:* $\max\limits_{1 \leq n \leq N_m} \| U_m^n \|_H^2 + \sum_{n=0}^{N_m-1} \tau_{m,n} \left\| \frac{U_m^{n+1} + U_m^n}{2} \right\|_V^2 \leq C\left(\| U_m^0 \|_H^2 + \sum_{n=0}^{N_m-1} \tau_{m,n}\left(1 + \| f_{m,h}(t_{m,n+1/2}) \|_{V_h{}'}^2\right)\right)$.

Proof.

Testing the discrete scheme (44) with $\phi_h = U_m^{n+1} + U_m^n$ yields the standard identity for the time derivative in H:

$$\left(\frac{U_m^{n+1} - U_m^n}{\tau_{m,n}}, U_m^{n+1} + U_m^n\right)_H = \frac{\| U_m^{n+1} \|_H^2 - \| U_m^n \|_H^2}{\tau_{m,n}} \quad (54)$$

Define the midpoint value by $U_m^{n+1/2} := \frac{1}{2}(U_m^{n+1} + U_m^n)$, the bilinear term satisfies the discrete Gårding inequality (D 4.2):

$$a_m\left(U_m^{n+\frac{1}{2}}, U_m^{n+1} + U_m^n\right) = 2a_m\left(U_m^{n+1/2}, U_m^{n+1/2}\right) \geq 2\alpha \| U_m^{n+1/2} \|_V^2 - 2\beta \| U_m^{n+1/2} \|_H^2. \quad (55)$$

Additionally, the midpoint value satisfies the standard convexity estimate:

$$\| U_m^{n+1/2} \|_H^2 \leq \frac{1}{2}(\| U_m^{n+1} \|_H^2 + \| U_m^n \|_H^2), \quad (56)$$

and therefore:

$$-2\beta \| U_m^{n+1/2} \|_H^2 \geq -\beta(\| U_m^{n+1} \|_H^2 + \| U_m^n \|_H^2). \quad (57)$$

For the nonlinear term, assumption D 4.4 together with Young's inequality gives, for any $\varepsilon > 0$,

$$\langle \mathcal{G}_{m,h}(U_m^{n+1}) + \mathcal{G}_{m,h}(U_m^n), U_m^{n+1/2} \rangle_{V_h{}', V_h} \leq C_G(1 + \| U_m^{n+1} \|_H + \| U_m^n \|_H) \| U_m^{n+1/2} \|_V \quad (58)$$

$$\leq \varepsilon \parallel U_m^{n+1/2} \parallel_V^2 + C_\varepsilon (1 + \parallel U_m^{n+1} \parallel_H^2 + \parallel U_m^n \parallel_H^2). \quad (59)$$

Similarly, Cauchy-Schwarz and Young's inequality yield the bound for the forcing term:

$$\langle f_{m,h}(t_{m,n+1/2}), 2U_m^{n+1/2} \rangle_{V_h', V_h} \leq \varepsilon \parallel U_m^{n+1/2} \parallel_V^2 + C_\varepsilon \parallel f_{m,h}(t_{m,n+1/2}) \parallel_{V_h'}^2. \quad (60)$$

Collecting these algebraic bounds into the governing weak formulation and isolating the variables for the subsequent iteration $n+1$ establishes the structural stability limits:

$$\begin{aligned} &(1 - \tau_{m,n} C_\varepsilon{}') \parallel U_m^{n+1} \parallel_H^2 + 2\tau_{m,n}(\alpha - \varepsilon) \parallel U_m^{n+\frac{1}{2}} \parallel_V^2 \\ &\leq (1 + \tau_{m,n} C_\varepsilon{}') \parallel U_m^n \parallel_H^2 + \tau_{m,n} C_\varepsilon{}' (1 + \parallel f_{m,h} \parallel_{V_h'}^2), \end{aligned} \quad (61)$$

where $C_\varepsilon{}' := \max\{\beta, C_\varepsilon\}$. Choosing $\varepsilon = \alpha/2$gives $2(\alpha - \varepsilon) = \alpha > 0$.

To ensure positivity of the leading coefficient, define the stability threshold $\tau_{stab} := 1/(2C_{\alpha/2}{}')$ and impose the global restriction $\tau^\star := \min\{\tau_{solv}, \tau_{stab}\}$. For all steps satisfying $\tau_{m,n} \leq \tau^\star$, the leading coefficient satisfies $1 - \tau_{m,n} C_{\alpha/2}{}' \geq 1/2$. Dividing uniformly by this positive coefficient allows the direct application of the discrete Gronwall lemma across the sequential summation $n = 0, \dots, N_m - 1$, completing the interval-wise conditional stability proof. □

Corollary 5.1 (Global Stability Across Switching Times). *If the hypotheses of Theorem 5.1 hold dynamically on every isolated spatial-temporal interval, and the strict continuity initialization condition* $U_{m+1}^0 = U_m^{N_m}$ *originating from (45) is applied, the defined scheme yields a global stability bound:* $\max_{1 \leq m \leq M} \max_{0 \leq n \leq N_m} \parallel U_m^n \parallel_H^2 \leq C_T \left(\parallel U_1^0 \parallel_H^2 + \sum_{m=1}^{M} \sum_{n=0}^{N_m - 1} \tau_{m,n} \left(1 + \parallel f_{m,h}(t_{m,n+1/2}) \parallel_{V_h'}^2 \right) \right)$.

Proof.

Because the final nodal matrix value characterizing the end of interval I_m matches the initial condition demanded by interval I_{m+1}, the interval-wise estimates extend across the partition points. The constant C_T depends on the final time Tthrough the discrete Gronwall argument, but it is independent of the mesh parameter $h$and the time step τ. □

5.2. Consistency and Convergence Verification

To separate the spatial elliptic residual and obtain the optimal $O(h^{p+1})$ convergence rate in the L^2-norm without requiring complex Nitsche duality arguments, let $\Pi_h: V \to V_h$ denote the standard Ritz (elliptic) projection operator defined via the bilinear form $a_m(\Pi_h v, \phi_h) = a_m(v, \phi_h)$. Under standard elliptic regularity, this satisfies the optimal approximation estimate:

$$\parallel v - \Pi_h v \parallel_H + h \parallel v - \Pi_h v \parallel_V \leq C h^{p+1} \parallel v \parallel_{H^{p+1}}, \quad (62)$$

applicable to sufficiently smooth functions v, where $p \geq 1$denotes the polynomial degree of the finite-element space.

To define the nodal error, let

$$W_m^n := \Pi_h u(t_{m,n}), e_m^n := W_m^n - U_m^n. \quad (63)$$

The total nodal error then splits as: $u(t_{m,n}) - U_m^n = (u(t_{m,n}) - W_m^n) + e_m^n := \eta_m^n + e_m^n$.

Lemma 5.1 (Local Consistency Defect). *Assume the exact solution* u *satisfies* $u|_{I_m} \in C^3(I_m; V) \cap C^1(I_m; H^{p+1})$. *By inserting* $W_m^n = \Pi_h u(t_{m,n})$ *directly into the Crank-Nicolson formulation (44), the resulting local consistency defect* $R_m^{n+1/2} \in V_h'$ *satisfies:* $\parallel R_m^{n+1/2} \parallel_{V_h'} \leq C(\tau_{m,n}^2 + h^{p+1})$.

Proof.

The exact solution satisfies the continuous PDE. The residual $R_m^{n+1/2}$measures the discrepancy obtained when substituting the discrete spatial projection $W_m^n = \Pi_h u(t_{m,n})$ into the midpoint discrete operator. This residual consists of two components: a temporal quadrature defect and a spatial projection defect. A Taylor expansion about the midpoint time $t_{m,n+1/2}$ confirms that the differential derivative approximation alongside the trapezoidal integration averaging inject localized temporal errors bounded by $\mathcal{O}(\tau_{m,n}^2)$. Concurrently, the spatial defect injected by utilizing $\Pi_h u$ instead of u contributes an $\mathcal{O}(h^{p+1})$ error component via the spatial approximation properties of the conforming finite-element space (62). Combining these bounds yields the stated total defect limit. Consequently, local truncation error bounds obtained by Taylor expansion on each interval I_m remain valid directly up to the interface t_m. Because the discrete grid is constructed to terminate exactly at the interface, midpoint/trapezoidal approximations never evaluate across two different regimes, so the usual $\mathcal{O}(\tau^2)$ temporal consistency remains valid without interface-induced order reduction. □

Theorem 5.2 (Global Convergence on a Switching-Aware Grid).
Assume that u *is continuous in* H*at each switching time and that* $u\,|_{I_m} \in C^3(I_m;V)$ *for each* m. *Assume also that the conditional stability requirement of Theorem 5.1 holds, namely* $\tau_{m,n} \le \tau^\star$. *If the switching times coincide with grid nodes and the restart rule (45) is applied at each interface, then the fully discrete CN approximation converges globally without loss:* $\max_{1\le m\le M}\max_{0\le n\le N_m} \| u(t_{m,n}) - U_m^n \|_H \le C_T(\| u_0 - \Pi_h u_0 \|_H + h^{p+1} + \tau_{max}^2)$, *where* $\tau_{max} := max_{1\le m\le M} max_{0\le n\le N_m-1}\tau_{m,n}$, *and* C_T *depends on* T*and the structural constants, but is independent of* h*and* τ_{max}, *provided* $\tau_{max} \le \tau^\star$.

Proof.
By inserting the exact projection term W_m^n directly into the discrete operator structure, we define the exact residual equation governing the projection mapping:

$$\begin{aligned}\left(\frac{W_m^{n+1} - W_m^n}{\tau_{m,n}}, \phi_h\right)_H &+ a_m\left(\frac{W_m^{n+1} + W_m^n}{2}, \phi_h\right) + \frac{1}{2}\langle G_{m,h}(W_m^{n+1}) \\ &+ G_{m,h}(W_m^n), \phi_h\rangle_{V_h',V_h} = \langle f_{m,h}\left(t_{m,n+\frac{1}{2}}\right), \phi_h\rangle_{V_h',V_h} + \langle R_m^{n+\frac{1}{2}}, \phi_h\rangle_{V_h',V_h}.\end{aligned} \tag{64}$$

Subtracting the evaluated numerical scheme (44) sequentially from this mapped residual identity yields the discrete error equation for e_m^{n+1}:

$$\begin{aligned}&\left(\frac{e_m^{n+1} - e_m^n}{\tau_{m,n}}, \phi_h\right)_H + a_m\left(\frac{e_m^{n+1} + e_m^n}{2}, \phi_h\right) \\ &= \langle R_m^{n+\frac{1}{2}}, \phi_h\rangle_{V_h',V_h} - \frac{1}{2}\langle G_{m,h}(W_m^{n+1}) - G_{m,h}(U_m^{n+1}) + G_{m,h}(W_m^n) \\ &\qquad - G_{m,h}(U_m^n), \phi_h\rangle_{V_h',V_h}.\end{aligned} \tag{65}$$

Setting the test function to $\phi_h = e_m^{n+1} + e_m^n$, the time derivative term becomes $(\| e_m^{n+1} \|_H^2 - \| e_m^n \|_H^2)/\tau_{m,n}$. The nonlinear difference term is bounded using the Lipschitz condition (D 4.3). The resulting nonlinear difference sequence is bounded smoothly via the established Lipschitz condition (D 4.3):

$$\langle \mathcal{G}_{m,h}(W_m^{n+1}) - \mathcal{G}_{m,h}(U_m^{n+1}), e_m^{n+1} + e_m^n\rangle_{V_h',V_h} \le L_G \| e_m^{n+1} \|_H \| e_m^{n+1} + e_m^n \|_V. \tag{66}$$

Applying Young's inequality as in the stability proof absorbs the resulting terms. Under the condition $\tau_{m,n} \le \tau^\star$, the discrete Gronwall lemma then yields an interval-wise bound in terms of the initial error $\| e_m^0 \|_H^2$ and the accumulated residual norm $\| R_m^{n+1/2} \|_{V_h'}^2$, which Lemma 5.1 bounds by $\mathcal{O}(\tau_{max}^4 + h^{2p+2})$.

Upon intersecting a physical temporal interface at t_m, the continuous state transmission condition $(u(t_m^-) = u(t_m^+))$ completely synchronizes with the algorithmic restart rule, yielding the exact discrete error relation $e_{m+1}^0 = e_m^{N_m}$. Hence the local error bound carries from one interval to the next over $[0, T]$.. The inclusion of the bounded spatial projection error η_m^n then yields the stated global convergence bound. □

6. NUMERICAL VERIFICATION AND VALIDATION

This section examines temporal and spatial verification, nonlinear switching behavior, and computational efficiency. Before proceeding to the experiments, it is worth mentioning that all preceding arguments extend componentwise to vector-valued states $u: \Omega \to \mathbb{R}^q$ by replacing $H = L^2(\Omega)$ and $V = H_0^1(\Omega)$ with product spaces $H = L^2(\Omega)^q$ and $V = H_0^1(\Omega)^q$, and interpreting $a_m(\cdot,\cdot)$ and $\mathcal{G}_{m,h}(\cdot)$ accordingly. The Lipschitz/growth/energy-control assumptions are then imposed with respect to the induced product norms.

6.1. Verification of Temporal Order (ODE MMS)

We verify the second-order temporal convergence of the restarted IMEX solver using the scalar test problem:

$$\frac{du}{dt} = -u + \cos(t) + \sin(t), \quad u(0) = 0, \quad t \in [0,1], \tag{67}$$

yielding the exact reference solution $u(t) = \sin(t)$.
Let $E_\tau = \| U^N - u(T) \|$ denote the terminal error, and define the observed slope by $p_{\text{obs}} = \log_2(E_{2\tau}/E_\tau)$.

Table 1. Temporal convergence results for the IMEX solver applied to the MMS ODE problem (67).

Time Step (τ)	Absolute Error (E_τ)	Observed Order (p_{obs})
0.10000	4.2295e-04	–
0.05000	1.0564e-04	2.00
0.02500	2.6405e-05	2.00
0.01250	6.6010e-06	2.00
0.00625	1.6502e-06	2.00

The results reported in Table 1 are consistent with second-order temporal convergence for the restarted IMEX implementation. This behavior is consistent with the classical order properties of BDF2 combined with second-order explicit extrapolation on uniform grids. Classical BDF2 is A-stable and exhibits stronger practical damping than Crank-Nicolson, but it is not L-stable. This result complements the consistency analysis established for the baseline Crank-Nicolson scheme. To visually corroborate this asymptotic behavior, Figure 1 presents a log-log plot of the absolute terminal error E_τ against the time step size τ. The solid curve represents the computed solver error, while the dashed reference line denotes the ideal slope 2. As shown in the figure, the solver's error trajectory closely follows the reference slope as $\tau \to 0$. This agreement supports the conclusion that the restart mechanism preserves the expected second-order convergence of the IMEX-BDF2 formulation without evident interface-induced order degradation.

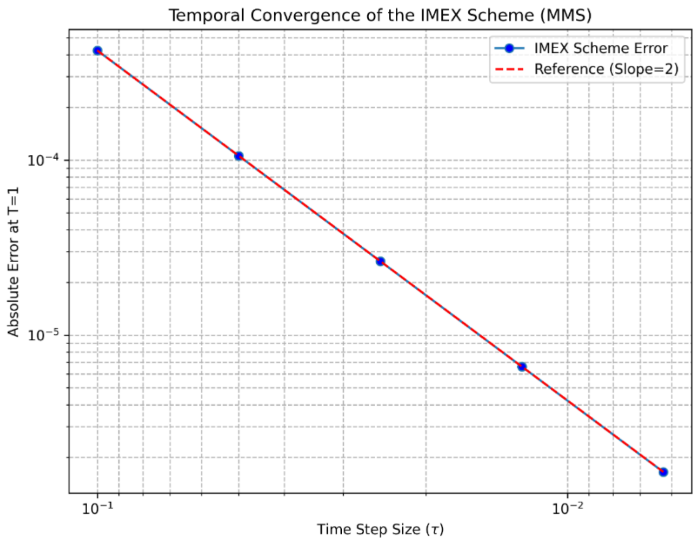

Figure 1. Log-log plot of the absolute error versus the time step τ for the temporal MMS test.

6.2. Verification of Spatial Order (FE Consistent)

To verify the spatial convergence rate of the finite-element discretization, we consider the one-dimensional heat equation

$$\partial_t u = \partial_{xx} u + S(x,t), x \in (0,1), t \in [0,1], \tag{68}$$

with exact solution $u(x,t) = \sin(\pi x)\cos(t)$.

For sufficiently smooth source terms, a conforming global Galerkin integration implies that the resulting L^2 error should scale as $\mathcal{O}(h^{p+1})$. In the present experiment we use cubic elements, so $p = 3$and fourth-order spatial convergence is expected.

To ensure that the temporal discretization error remains negligible relative to the spatial error, we choose $\tau = \mathcal{O}(h^{p+1})$ (where precisely $p = 3$). With this choice, the temporal contribution scales as $\mathcal{O}(h^8)$, so the measured L^2rate reflects the spatial discretization error.

Table 2. Spatial convergence results for the IMEX solver applied to the PDE problem (68) utilizing $p = 3$ FE.

N_x	Step Size (h)	L^2 Error (E_h)	Observed Order (p_{obs})
20	0.05000	6.9542e-08	–
40	0.02500	4.3453e-09	4.00
80	0.01250	2.7059e-10	4.01
160	0.00625	1.6912e-11	4.00

The results reported in Table 2 show a systematic reduction in the spatial error, with the error decreasing by approximately a factor of 16 under each mesh bisection. The observed rate remains near $p_{\text{obs}} = 4.00$, which is consistent with fourth-order spatial convergence for cubic elements. Figure 2 plots the L^2-error against the mesh size h on a log-log scale. This log-log plot tracks the L^2-norm error E_h against the spatial mesh size h. By choosing the temporal step $\tau = \mathcal{O}(h^4)$, the temporal error is kept small enough for the plot to primarily reflect the spatial discretization error. The resulting curve closely follows the $\mathcal{O}(h^4)$ reference slope across successive bisection intervals. Figure 2 therefore indicates that the integration framework supports high-order continuous piecewise polynomial elements ($p = 3$) without evident numerical distortion in this test.

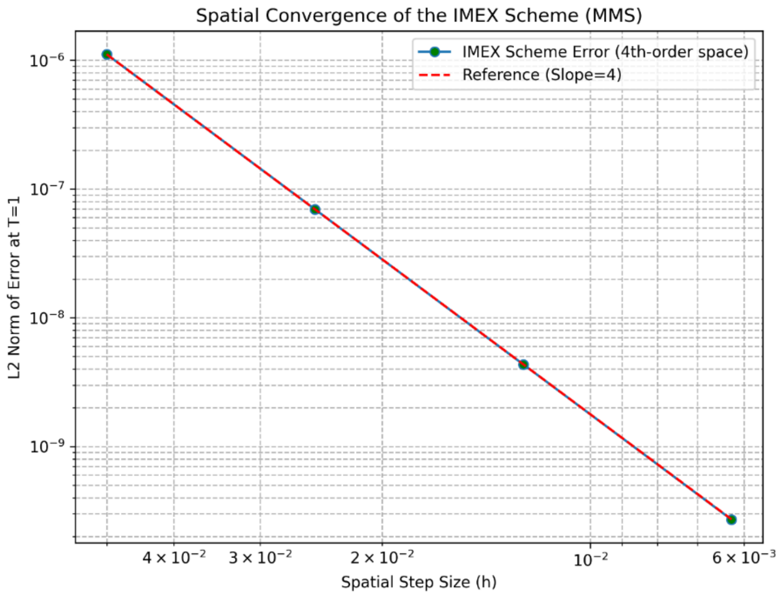

Figure 2. Log-log plot of the discrete L^2-error versus the spatial step size h for the spatial MMS test.

6.3. Validation: Switching Lotka-Volterra Reaction-Diffusion (Dirichlet Consistent)

Although Lotka-Volterra reactions are not globally Lipschitz, our computations are consistent with Assumption A 2.4 by using a standard truncation $\mathcal{G}^{\mathrm{R}}$ (which coincides with $\mathcal{G}$ on the numerically observed bounded trajectory), or equivalently by operating in a regime where the solution remains uniformly bounded so that the reaction map is effectively Lipschitz on the attained range.

To illustrate the behavior of the method in a nonlinear switching setting, we consider a one-dimensional Lotka-Volterra reaction-diffusion system on $\Omega = (0,1)$, with parameters that change across two temporal phases $m \in \{1,2\}$:

$$\partial_t u \quad = D_{u,m}\, \partial_{xx} u + \alpha_m u - \beta_m uv, \tag{69}$$

$$\partial_t v \quad = D_{v,m}\, \partial_{xx} v + \delta_m uv - \gamma_m v, \tag{70}$$

subject to homogeneous Dirichlet boundary conditions, consistent with the choice $V = H_0^1(\Omega)$:

$$u(0,t) = u(1,t) = 0, \qquad v(0,t) = v(1,t) = 0, \qquad t \in [0,200]. \tag{71}$$

We introduce a switching time at $t_1 = 50$, at which the reaction parameters change instantaneously to represent a regime transition:

Phase 1: baseline biological growth $(t \in [0,50))(\alpha_1 = 2.0)$, predator mortality $(\gamma_1 = 1.0)$, and diffusivities $D_{u,1} = D_{v,1} = 0.01$.

Phase 2: increased conversion rate $(t \in [50,200])(\delta_2 = 1.5)$, reduced predator mortality $(\gamma_2 = 0.75)$, and diffusivities $D_{u,2} = D_{v,2} = 0.01$.

This parameter change increases the predator conversion rate $(\delta_1 \to \delta_2)$and decreases predator mortality $(\gamma_1 \to \gamma_2)$, thereby moving the system into a different dynamical regime. Figure 3 shows the population densities over $t \in [0,200]$, with the switching time indicated by a vertical dashed line at $t_1 = 50$. Before the interface, the solution exhibits stable oscillatory behavior. After the switch, the solver transitions smoothly to the new regime without visible interface artifacts.

Figure 3 shows no visible numerical spikes or boundary-layer artifacts at the switching time $t_1 = 50$, which is consistent with the role of the restart strategy in preventing interface-induced contamination.

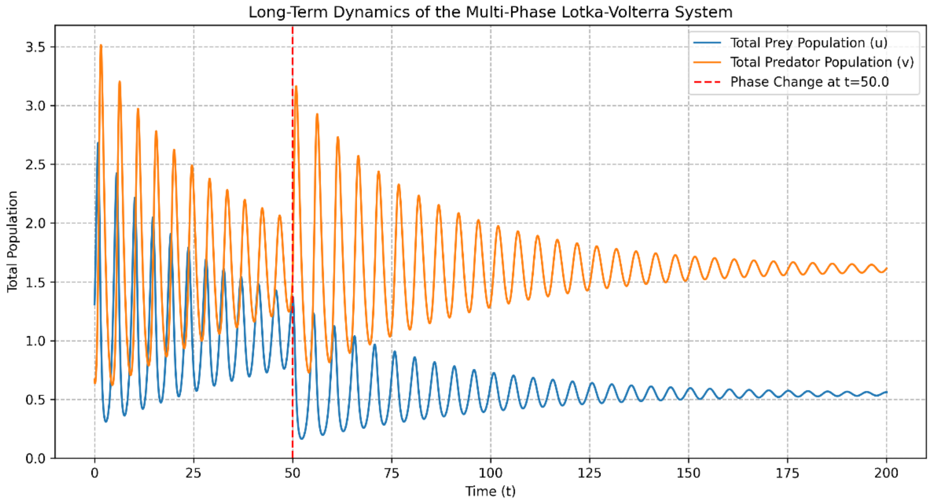

Figure 3. Long-term evolution of total prey (blue) and predator (red/orange) populations in the multiphase Lotka-Volterra system.

In Phase 2, the increased value of $\delta_2$drives the populations toward a different oscillatory regime with a shorter apparent period. To further examine this transition, Figure 4 plots the same system in phase space, with predator density $v(t)$against prey density $u(t)$. The phase portrait shows two distinct dynamical regimes. The outer loop corresponds to the Phase 1 limit cycle, whereas the inner loop corresponds to the faster Phase 2 dynamics after the parameter jump. The figure indicates that the solver preserves the phase-space structure of both regimes without visible distortion caused by cross-interface interpolation.

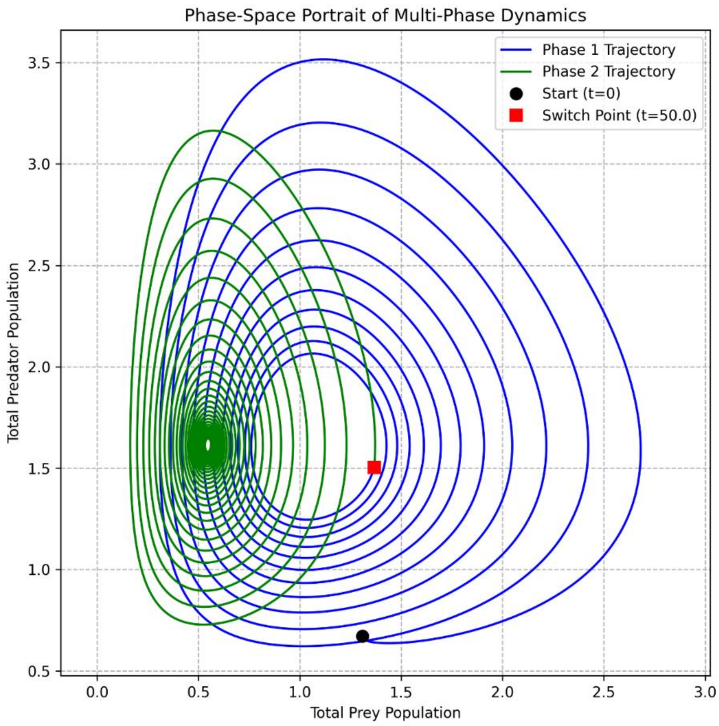

Figure 4. Phase-space portrait of the multiphase Lotka-Volterra system.

To further assess the numerical behavior of the scheme, Figure 5 tracks the discrete L^2-norm of the system state over the simulation interval. In nonlinear reaction systems, operator jumps can lead to sharp changes in the solution norm. In Figure 5, the computed norm remains bounded and passes smoothly through the $t_1 = 50$ interface without signs of rapid growth. This energy trace is consistent with the conditional stability analysis for the baseline scheme.

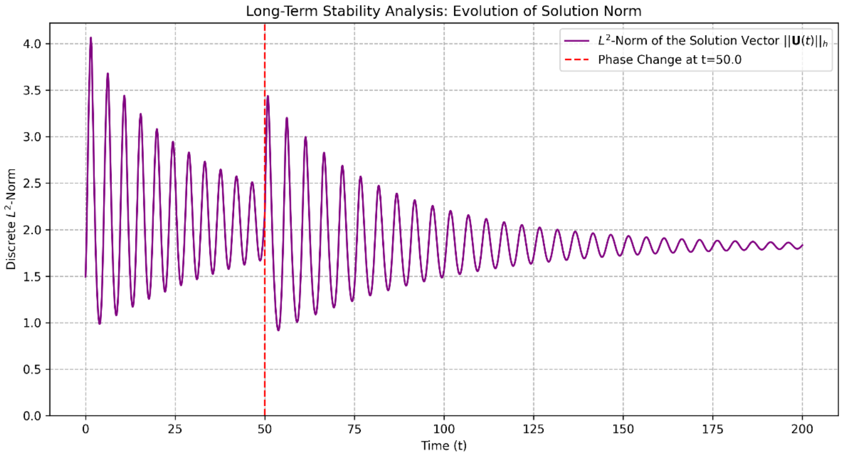

Figure 5. Evolution of the discrete L^2-norm of the solution vector for the multiphase Lotka-Volterra system.

6.4. Application: Multiphase Heat Conduction with Diffusion Jump

To examine the method in a stiff linear setting, we consider a one-dimensional heat equation with a diffusion coefficient that changes abruptly in time:

$$\partial_t u = D_m \partial_{xx} u, \quad x \in (0,1), \quad t \in [0,1], \tag{72}$$

The problem is subject to the boundary conditions $u(0,t) = u(1,t) = 0$ and the initial condition $u(x,0) = \sin(\pi x)$. The time interval is split at $t_1 = 0.1$:

Phase 1: $(t < 0.1) D_1 = 0.1$.

Phase 2: $(t \geq 0.1) D_2 = 1.0$.

This tenfold increase in diffusivity introduces a sharp change in stiffness. Figure 6 shows solution profiles immediately before and after the transition at $t_1 = 0.1$. Before the switch, the decay is gradual; after the switch, the larger diffusion coefficient produces faster smoothing. The spatial profiles remain smooth, and no visible numerical ringing is observed near the boundaries.

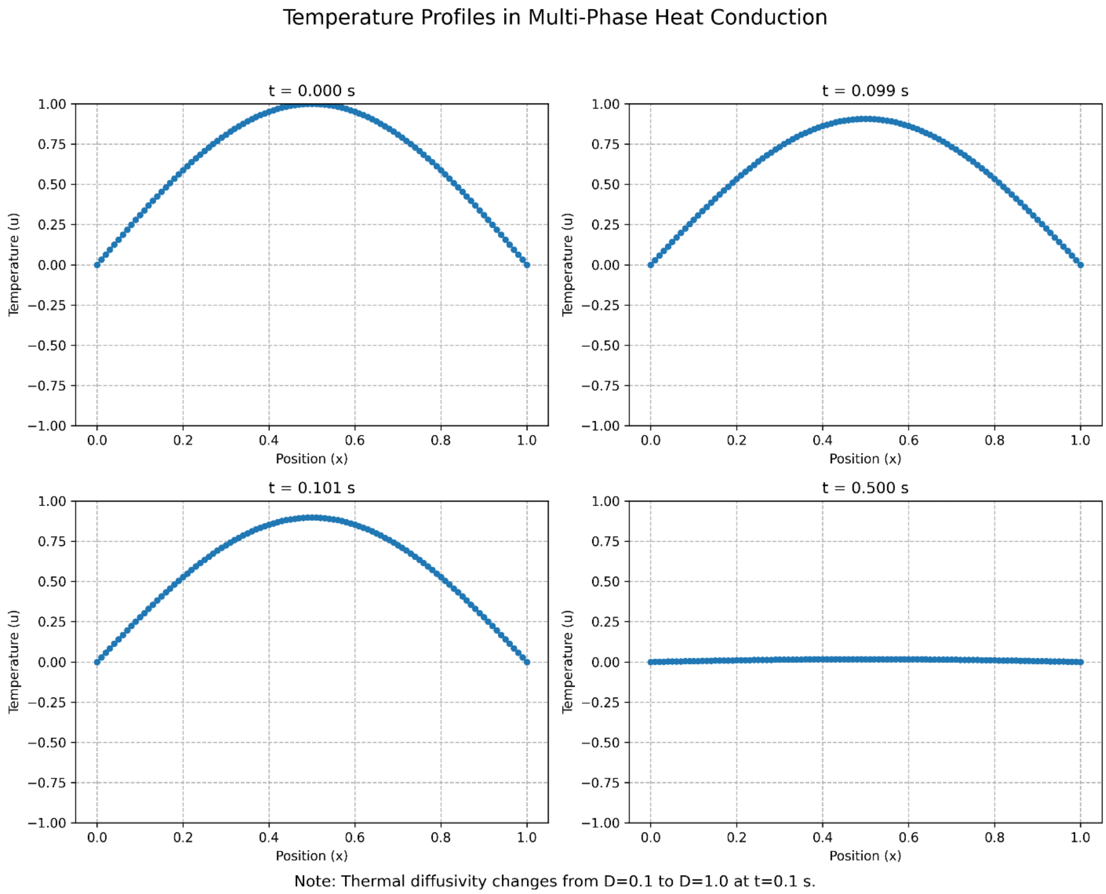

Figure 6. Temperature profiles for the multiphase heat conduction problem at four key time points.

This configuration is intended to represent a phase-change-type diffusion jump with increased stiffness. In this setting, an explicit time integrator is subject to a stability restriction of the form $\tau_{\max} \propto h^2$. Figure 7 illustrates this restriction for a standard Forward Euler discretization of the same discontinuous problem. The plot shows the maximum stable time step $\tau_{\max}$ versus the mesh size h, and the observed decay is consistent with the relation $\tau_{\max} \propto h^2$. After the transition to Phase 2, the stable operating region shifts downward, showing that the explicit method becomes more restrictive in this regime. Because the spectral radius of the diffusion operator controls stability, the tenfold increase in D reduces the allowable time step by a comparable factor.

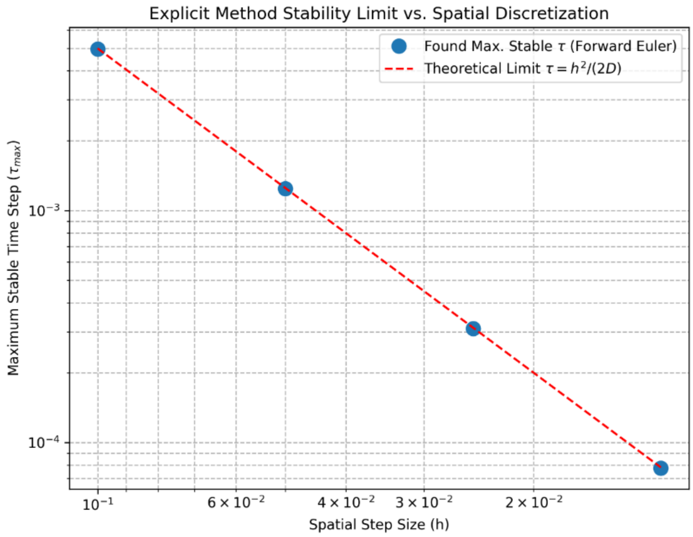

Figure 7. The maximum stable time step ($\tau_{\max}$) for the Forward Euler explicit scheme as a function of spatial step size (h).

To illustrate the effect of violating this stability restriction, Figure 8 provides a side-by-side comparison. The plot overlays the stable IMEX-BDF2 solution with an explicit Forward Euler solution computed with the same time step ($\tau = 0.001$) immediately after the phase boundary. As shown in Figure 8, the explicit solution rapidly becomes unstable, whereas the IMEX formulation remains stable over the reported time window.

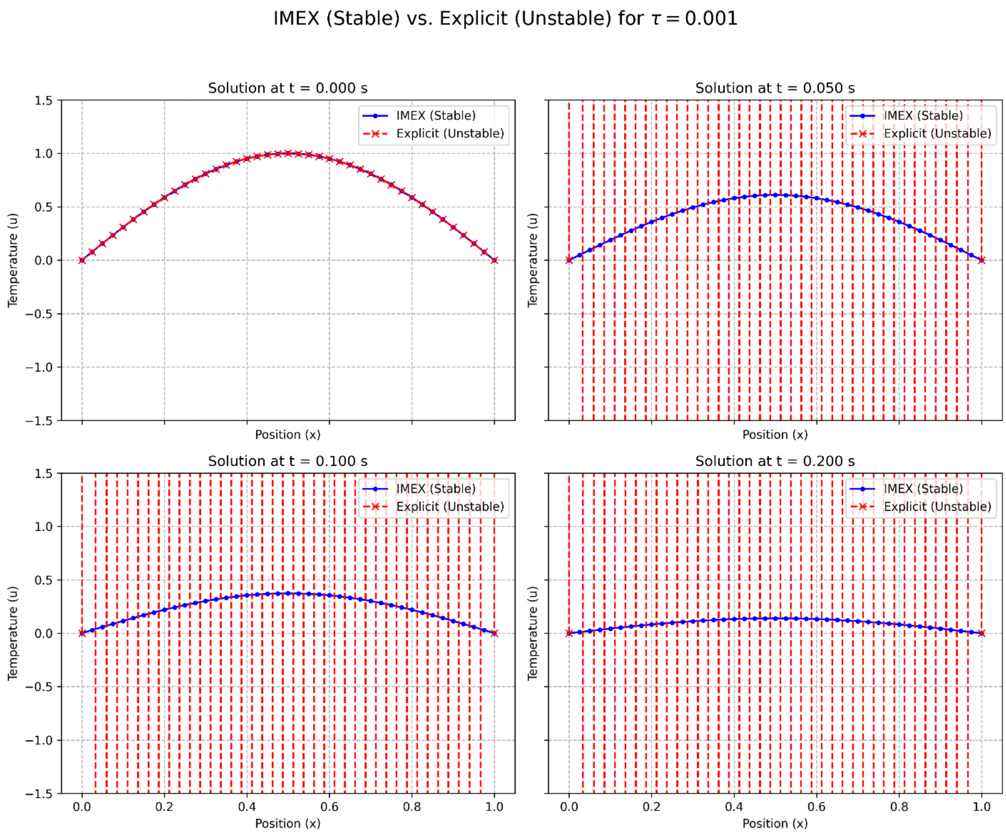

Figure 8. Direct comparison of the stable IMEX solution (blue solid line) and the unstable Forward Euler solution (red dashed line) for a stiff problem configuration ($\tau = 0.001$).

6.5. Generalization to 2D and Algorithmic Efficiency

We next extend the test problem to two spatial dimensions to examine whether the solver remains effective in a higher-dimensional setting. The corresponding multiphase model is posed on the unit square, with the switching time shifted to $t_1 = 0.05$. Figure 9 presents contour plots of the temperature field at several representative times, including the initial state, the switching interface, and the final state. The contours remain smooth and symmetric throughout the computation, and no visible directional bias or interface-induced distortion is observed in this example.

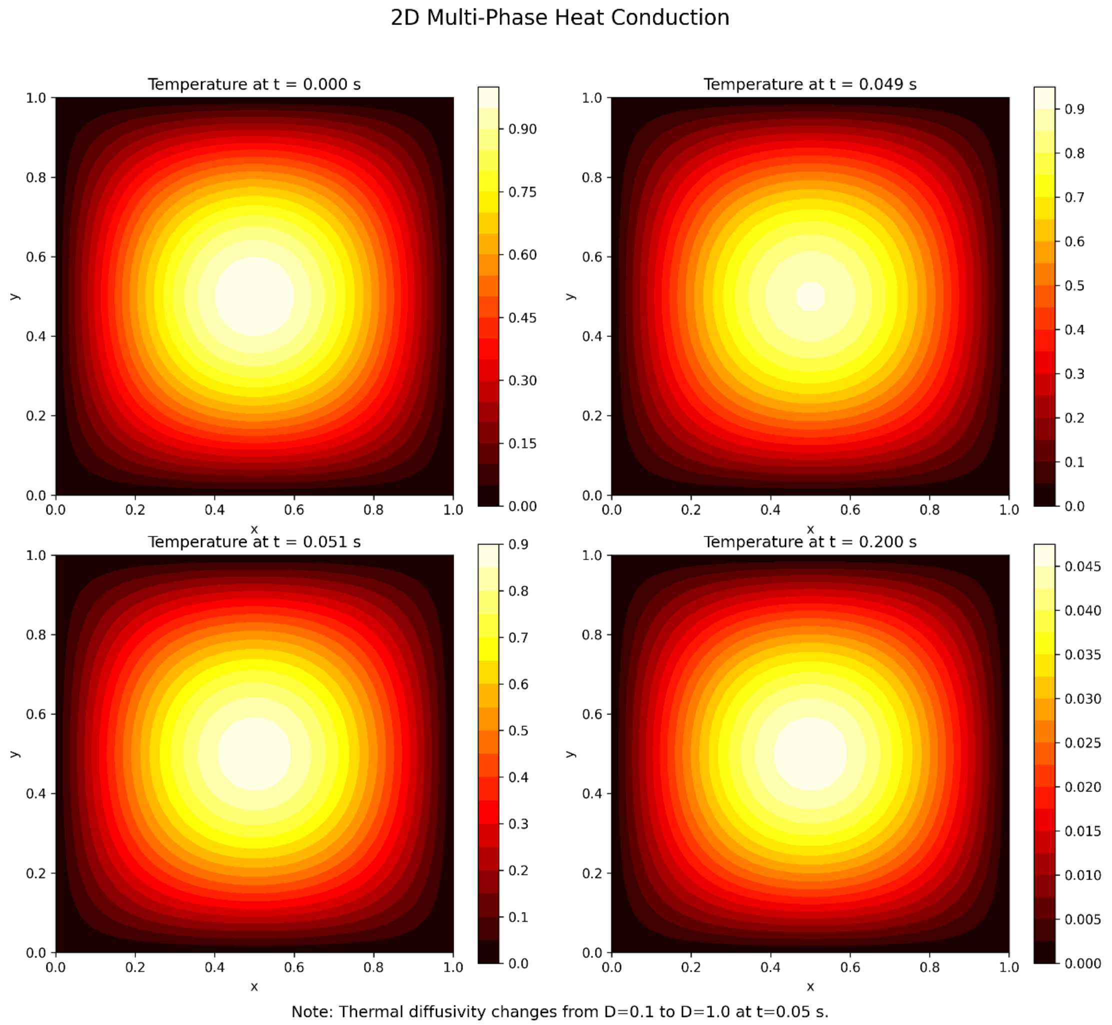

Figure 9. Temperature distribution for the 2D multiphase heat conduction problem at four key time points.

The computational efficiency of the restarted implementation is illustrated in Figure 10. This work-precision diagram plots the terminal error against the measured CPU time. The figure compares the interval-restarted IMEX-BDF2 configuration with a non-restarted classical BDF2 solver applied to the same discontinuous PDE. In the reported tests, the restarted strategy shifts the work-precision curve toward lower cost for comparable accuracy, indicating a favorable efficiency trade-off for this class of problems.

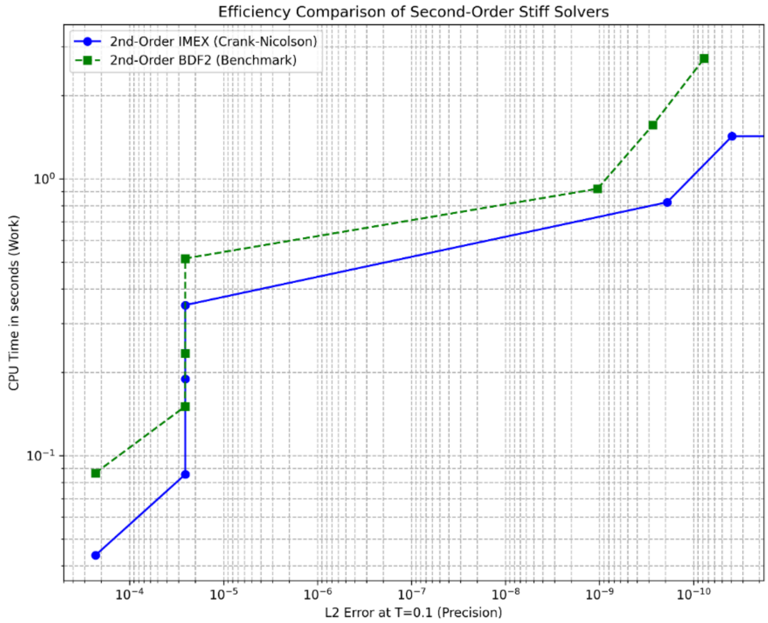

Figure 10. Work-precision diagram comparing the computational efficiency of the proposed 2nd-order IMEX scheme against the classical 2nd-order BDF2 scheme for the 1D heat problem.

7. DISCUSSION

The results of this study indicate that an interval-wise framework provides a mathematically consistent approach for treating semilinear parabolic equations with piecewise-in-time operators. Section 3 establishes global weak well-posedness by solving the problem on successive time slabs and transmitting the state continuously in the pivot space H, thereby matching the discontinuous temporal structure of the model. This continuous formulation provides the theoretical basis for the switching-aware numerical strategy developed and tested in the latter half of the paper.

The numerical experiments are consistent with that analytical framework. In particular, the switching-aware time grid and the restart mechanism preserve the expected temporal accuracy while reducing the history-mixing effects that may arise when standard multistep schemes cross a genuine switching interface. The validation experiments also indicate that the restart strategy performs reliably in the nonlinear and stiff settings examined here. In the multiphase Lotka-Volterra ecosystem, the algorithm passes through the switching time without generating spurious temporal layers. In the heat-conduction example, the method remains stable across a sharp diffusion jump, whereas an unshielded explicit treatment becomes strongly constrained by CFL-type limits.

These observations are consistent with several computational difficulties highlighted in comparative studies of second-order stiff solvers. Classical methods such as Crank-Nicolson may respond to jump discontinuities with persistent and weakly damped high-frequency oscillations (Østerby, 2003), while standard BDF2 formulations may be sensitive to start-up errors and energy growth near interfaces (Nishikawa, 2019). More broadly, the stiff-integration literature has shown that low regularity, incompatibility conditions, and defect accumulation can affect the observed order and damping behavior of higher-order schemes (Auzinger & Herfort, 2014; Auzinger et al., 2014, 2015; Hansen & Ostermann, 2016; Alonso-Mallo et al., 2017a, 2017b; Hochbruck et al., 2020; Cano & Reguera, 2022). Recent work has attempted to address related difficulties using more elaborate stabilization devices, including penalty-based Lagrange multipliers (Hou et al., 2023), dual Schur domain decompositions (Brun et al., 2015), and specialized Scalar Auxiliary Variable constructions (Zhang et al., 2025) to enforce interface continuity and suppress spurious pseudo-energy. In comparison with those approaches, the present results suggest that, in the specific setting of prescribed temporal operator switching, a simpler phase-aware restart principle can already reduce cross-interface reuse of multistep information.

Within these limits, the results suggest a practical implication. When temporal interfaces are genuine modeling features rather than numerical artifacts, it is beneficial to represent them explicitly at both the continuous and discrete levels. The interval-wise weak theory respects the slab structure of the problem, while the restart rule prevents multistep or multistage memory from blending information generated under incompatible operators. In this sense, the proposed framework may be viewed not merely as a coding adjustment, but as a discretization principle aligned with the transmission structure of the underlying model.

8. LIMITATIONS AND FUTURE RESEARCH DIRECTIONS

8.1. Analytical and Nonlinear Scope

The scope and boundaries of the present work should also be stated carefully. The current analytical framework assumes that the switching instants $\{t_m\}$ are prescribed a priori and do not depend on the evolving state. While this covers a broad class of scheduled multiphase phenomena, many complex systems feature state-triggered switching, for example, when a transition occurs only after a threshold condition has been reached. Extending the present piecewise weak formulation to accommodate state-dependent switching would require the incorporation of more advanced event-location and time-transformation techniques, including methods developed for differential-algebraic settings (Lopez & Maset, 2024).

A further analytical limitation concerns the class of nonlinearities treated in the paper. The well-posedness and discrete analysis adopt a globally Lipschitz assumption for the mapping $H \to V'$. While certain locally Lipschitz polynomial reactions may be handled through truncation or related arguments, highly singular or non-convex energy potentials, such as those arising in some Cahn-Hilliard or Allen-Cahn phase-field models, fall outside the present scope. For this reason, the current analysis should be understood as a structured first step rather than as a complete treatment of all switching parabolic systems.

8.2. Numerical and Discretization Limits

The full convergence theory established in this paper is proved for the interval-wise Crank-Nicolson method. By contrast, the restarted IMEX-BDF2 scheme is introduced primarily as a practical alternative for stiff regimes and is assessed through local consistency arguments, manufactured-solution verification, validation examples, and work-precision experiments. Accordingly, the numerical evidence supports its effectiveness for the switching problems considered here, but the paper does not claim a complete abstract convergence theory for restarted IMEX-BDF2 under the full generality of the continuous model.

In addition, to preserve the standard constant-coefficient BDF2 formulation without introducing further instability mechanisms, a uniform step size τ_m is imposed within each interval I_m. Recent studies show that variable-step BDF2 methods require strict adjacent step-ratio constraints, such as $r_k = \tau_k/\tau_{k-1} < 4.8645$, in order to preserve energy dissipation properties (Zhao et al., 2025; Liao & Zhang, 2021). The present algorithm avoids this complication by using a uniform inner step, but this reduces adaptivity within each slab.

The convergence proofs also rely on the assumption that the spatial mesh remains fixed. Extending the current framework to non-conformal interfaces, moving boundaries, or dynamically evolving geometries would require coupling the time-stepping logic with more advanced interface-capturing techniques, such as directional ghost-cell methods or particle level-set frameworks (Boniou et al., 2022).

The validation strategy should also be interpreted within its intended scope. Although the formulation accommodates heterogeneous spatial transmission, the numerical tests remain intentionally modest and are designed mainly to isolate the temporal-interface mechanism rather than to claim broad superiority across all stiff parabolic settings.

8.3. Future Research Directions

These limitations point naturally to several directions for further work. A first direction is the development of a complete abstract convergence and stability theory for restarted IMEX multistep schemes under prescribed switching. A second is the extension of the restart principle to adaptive event detection, variable-step restart logic, and more general switching criteria where the interface is not known in advance.

A further direction is the integration of the switching-aware restart methodology with stabilization techniques designed for strongly nonlinear systems, including Scalar Auxiliary Variable (SAV) and Invariant Energy Quadratization (IEQ) approaches (Zhang et al., 2025; Wang & Yu, 2018), which may offer a route toward unconditional energy stability for piecewise non-convex potentials. Additional work may also incorporate space-time adaptive refinement strategies (Pan et al., 2022) and variable-step IMEX formulations subject to the relevant step-ratio constraints.

Finally, it may be worthwhile to explore whether the interval-wise transmission philosophy developed here can be connected with broader verification and safety-assurance frameworks for hybrid cyber-physical systems (Wilson et al., 2025). At present, this remains a possible interdisciplinary direction rather than a claim of immediate applicability.

9. CONCLUSION

This paper developed a switching-aware analytical and numerical framework for semilinear parabolic equations with piecewise-in-time operators and prescribed switching times. At the continuous level, the model was formulated as an interval-wise variational problem on successive time slabs, with transmission enforced through continuity in the pivot space H at each switching instant. Under uniform ellipticity and standard nonlinear control assumptions, this structure allowed the global problem to be treated as a concatenation of slab-wise weak problems, yielding existence and uniqueness in a form adapted to the discontinuous temporal setting.

At the discrete level, the paper identified a central numerical difficulty associated with switching problems: standard multistep or multistage schemes may inadvertently reuse previously computed values generated under different operators when a temporal stencil crosses a genuine switching interface. To address this issue, a switching-aware restart principle was introduced, in which each switching time is enforced as an exact grid node and the time integrator is restarted from the transmitted state. This principle was implemented through an interval-wise Crank-Nicolson discretization, for which solvability, conditional stability, and convergence were established, and through a restarted IMEX-BDF2 variant, bootstrapped by one Crank-Nicolson step on each slab, intended as a practical alternative for stiff computations.

The numerical experiments support the relevance of this interface-safe strategy for the classes of examples studied here. Manufactured-solution tests confirmed the expected accuracy behavior of the baseline method, while the validation examples showed that the restarted algorithm can traverse prescribed switching times without the spurious temporal layers, start-up contamination, or interface-driven instability often associated with unprotected multistep history reuse.

Taken together, the contribution of the paper is twofold. First, it provides a mathematically consistent weak framework for semilinear parabolic equations with prescribed temporal operator switching. Second, it shows that the transmission structure of the continuous problem naturally motivates a restart rule at the discrete level that prevents cross-interface contamination of multistep history. Within the scope considered here, the results suggest that temporal interfaces in piecewise-in-time parabolic problems are better treated as structural features of the model rather than as small perturbations of a globally smooth evolution.

Nomenclature

The primary notations and mathematical symbols used in this paper are defined as follows:

Symbol	Description
T	Final simulation time for the global temporal domain $[0, T]$.
M	Total number of temporal subintervals (representing distinct operational phases).
$0 = t_0 < \cdots < t_M = T$	Discrete switching times representing temporal interfaces.
I_m	The m-th temporal subinterval, defined as the half-open set $(t_{m-1}, t_m]$.
$\Omega \subset \mathbb{R}^d$	Bounded spatial domain, with spatial dimension $d \geq 1$.
Ω_r	Spatial subdomains representing heterogeneous media geometries ($r = 1, \dots, R$).
Γ	Internal static spatial interface set separating adjacent subdomains.
$u(x, t)$	State variable (scalar focus; extension to multi-component systems is discussed).
$V \hookrightarrow H \hookrightarrow V'$	Gelfand triple: $V = H_0^1(\Omega)$, $H = L^2(\Omega)$, and V' is the topological dual of V.
$\langle \cdot, \cdot \rangle_{V', V}$	The standard duality pairing strictly between the spaces V' and V.
$(\cdot, \cdot)_H$	The standard L^2 inner product evaluated on the pivot space H.
$a_m(\cdot, \cdot)$	Bilinear form associated with the active linear elliptic operator on I_m.
$\mathcal{A}_{m,r}$	Active linear elliptic differential operator on subdomain Ω_r during interval I_m.
$K_{m,r}(x)$	Spatially dependent symmetric diffusion tensor, possibly jumping at t_m.
λ, Λ	Uniform lower and upper bounding constants ensuring strict spatial ellipticity.
$\mathcal{G}_{\sigma(m)}$	Globally assembled active nonlinear response operator assigned during interval I_m.
L_G, C_G	The global Lipschitz constant and linear growth bound defining the nonlinearity.
α, β	Coercivity and energy bounds defining the discrete Gårding inequality.
$f_m(t)$	Prescribed globally assembled external source term mapping into V' on I_m.
$\tau_{m,n}, \tau_m$	Local numerical time step size within interval I_m (uniform τ_m for multistep).
U_m^n	Fully discrete numerical approximation of the state u evaluated at time $t_{m,n}$.
$V_h, {V_h}'$	Conforming Finite Element functional space ($V_h \subset V$) and its algebraic dual.
Π_h	Spatial projection operator (Ritz projection) mapping the continuous state onto V_h.
W_m^n	Discrete nodal projection, $W_m^n := \Pi_h u(t_{m,n})$.
e_m^n	Discrete nodal numerical error, formally defined as $W_m^n - U_m^n$.

References

Alonso-Mallo, I., Cano, B., Reguera, N., 2017a. Analysis of order reduction when integrating linear initial boundary value problems with Lawson methods. Applied Numerical Mathematics 118, 64–74.

Alonso-Mallo, I., Cano, B., Reguera, N., 2017b. Avoiding order reduction when integrating linear initial boundary value problems with Lawson methods. IMA Journal of Numerical Analysis 37(4), 2091–2119.

Ascher, U. M., Ruuth, S. J., Spiteri, R. J., 1997. Implicit-explicit Runge-Kutta methods for time-dependent partial differential equations. Applied Numerical Mathematics 25(2–3), 151–167.

Auzinger, W., Herfort, W., 2014. Local error structures and order conditions in terms of Lie elements for exponential splitting schemes. Opuscula Mathematica 34(2), 243–255.

Auzinger, W., Koch, O., Thalhammer, M., 2014. Defect-based local error estimators for splitting methods, with application to Schrödinger equations, Part II. Higher-order methods for linear problems. Journal of Computational and Applied Mathematics 255, 384–403.

Auzinger, W., Koch, O., Thalhammer, M., 2015. Representation of the local error for higher-order exponential splitting schemes involving two or three sub-operators. AIP Conference Proceedings 1648(1), Article 150003.

Boniou, V., Schmitt, T., Vié, A., 2022. Consistency and accuracy in the simulation of two-phase flows with phase change using sharp interface capturing methods. Journal of Computational Physics 470, 111604.

Brun, M., Gravouil, A., Combescure, A., 2015. Heterogeneous asynchronous time integrators built from the energy method for coupling Newmark and α-schemes. COUPLED PROBLEMS 2015 – Proceedings of the 6th International Conference on Coupled Problems in Science and Engineering, 242–253.

Cano, B., Reguera, N., 2022. How to avoid order reduction when Lawson methods integrate nonlinear initial boundary value problems. BIT Numerical Mathematics 62(2), 431–463.

Creo, S., Lancia, M. R., Vernole, P., 2022. Transmission problems for the fractional p-Laplacian across fractal interfaces. Discrete and Continuous Dynamical Systems – Series S 15(12), 3621–3644.

Dong, H., Xu, L., 2021. Gradient estimates for divergence form parabolic systems from composite materials. Calculus of Variations and Partial Differential Equations 60(3), Article 98.

Edwan, R., 2022. On the construction of the implicit finite difference schemes for solving a time-space fractional convection-diffusion equation. University of Ha'il Journal of Science 3(1).

Feng, X., Shen, J., 1999. The finite element method for semilinear parabolic equations with discontinuous coefficients. Journal of Computational Mathematics 17(2), 191–198.

Fish, A. C., Reynolds, R. D., Roberts, S. B., 2024. Implicit–explicit multirate infinitesimal stage-restart methods. Journal of Computational and Applied Mathematics 438, 115534.

Gal, C. G., Warma, M., 2016. Transmission problems with nonlocal boundary conditions and rough dynamic interfaces. Nonlinearity 29(1), 161–197.

Gal, C. G., Warma, M., 2017. Nonlocal transmission problems with fractional diffusion and boundary conditions on non-smooth interfaces. Communications in Partial Differential Equations 42(4), 579–625.

Hansen, E., Ostermann, A., 2016. High-order splitting schemes for semilinear evolution equations. BIT Numerical Mathematics 56(4), 1303–1316.

Hochbruck, M., Leibold, J., Ostermann, A., 2020. On the convergence of Lawson methods for semilinear stiff problems. Numerische Mathematik 145(3), 553–580.

Hou, D., Ning, Y., Zhang, C., 2023. An efficient and robust Lagrange multiplier approach with a penalty term for phase-field models. Journal of Computational Physics 488, 112236.

Kadioglu, S. Y., 2017. Analysis of the self-consistent IMEX method for tightly coupled non-linear systems. Journal of Computational and Applied Mathematics 322, 148–160.

Liao, H.-L., Zhang, Z., 2021. Analysis of adaptive BDF2 scheme for diffusion equations. Mathematics of Computation 90(329), 1207–1226.

Lopez, L., Maset, S., 2024. Time reparametrization and event location for discontinuous differential algebraic equations. Journal of Scientific Computing 100(1), Article 3.

Matioc, B.-V., Walker, C., 2024. Well-posedness of quasilinear parabolic equations in time-weighted spaces. Proceedings of the Royal Society of Edinburgh Section A: Mathematics, 1–35.

Nishikawa, H., 2019. On large start-up error of BDF2. Journal of Computational Physics 392, 456–461.

Østerby, O., 2003. Five ways of reducing the Crank-Nicolson oscillations. BIT Numerical Mathematics 43(4), 811–822.

Pan, Y., Yan, Z.-G., Peiró, J., Sherwin, S. J., 2022. Development of a balanced adaptive time-stepping strategy based on an implicit JFNK-DG compressible flow solver. Communications on Applied Mathematics and Computation 4(2), 728–757.

Peterson, K., Bochev, P., Kuberry, P., 2019. Explicit synchronous partitioned algorithms for interface problems based on Lagrange multipliers. Computers and Mathematics with Applications 78(2), 459–482.

Schmitz, L. S., Walker, C., 2025. Recovering initial states in semilinear parabolic problems from time-averages. Journal of Differential Equations 429, 503–528.

Seibold, B., Shirokoff, D., Zhou, D., 2019. Unconditional stability for multistep IMEX schemes: practice. Journal of Computational Physics 376, 295–321.

Vynnycky, M., Mitchell, S. L., 2013. On the accuracy of a finite-difference method for parabolic partial differential equations with discontinuous boundary conditions. Numerical Heat Transfer, Part B: Fundamentals 64(4), 275–292.

Wang, D., Ruuth, S. J., 2008. Variable step-size implicit–explicit linear multistep methods for time-dependent partial differential equations. Journal of Computational Mathematics 26(6), 838–855.

Wang, H., Li, F., Shu, C.-W., Zhang, Q., 2023. Uniform stability for local discontinuous Galerkin methods with implicit-explicit Runge-Kutta time discretizations for linear convection-diffusion equation. Mathematics of Computation 92(344), 2475–2513.

Wang, L., Yu, H., 2018. On efficient second order stabilized semi-implicit schemes for the Cahn–Hilliard phase-field equation. Journal of Scientific Computing 77(2), 1185–1209.

Wang, W., Chen, Y., Fang, H., 2019. On the variable two-step IMEX BDF method for parabolic integro-differential equations with nonsmooth initial data arising in finance. SIAM Journal on Numerical Analysis 57(3), 1289–1317.

Wilke, M., 2023. Linear and quasilinear evolution equations in the context of weighted spaces. Archiv der Mathematik 121(5–6), 625–642.

Wilson, K., Al Arafat, A., Baugh, J., Yu, R., Liu, X., Guo, Z., 2025. Soteria: a formal digital-twin-enabled framework for safety-assurance of latency-aware cyber-physical systems. Proceedings of the 28th International Conference on Hybrid Systems, Article 22, 1–11.

Zhang, B., Fu, H., Lan, R., Xie, S., 2025. Energy dissipation law and maximum bound principle-preserving linear BDF2 schemes with variable steps for the Allen–Cahn equation. Journal of Scientific Computing 105(2), Article 51.

Zhao, C., Yang, R., Di, Y., Zhang, J., 2025. Sharp error estimate of variable time-step IMEX BDF2 scheme for parabolic integro-differential equations with initial singularity arising in finance. Journal of Computational Mathematics 43(5), 1118–1140.